Bi-modal deformation styles in confined mass-transport deposits: examples from a salt minibasin in SE Brazil

Davide Gamboa[1], Tiago M. Alves[2*]

[1]: British Geological Survey, Columbus House, Tongwynlais, Cardiff, CF15 7NE, United Kingdom

[2]: 3D Seismic Lab, School of Earth and Ocean Sciences, Cardiff University, Main Building, Park Place, Cardiff, CF10 2AT, United Kingdom

*Corresponding author: AlvesT@cardiff.ac.uk

Abstract

High-quality 3D seismic data reveal bi-modal deformation styles in mass-transport deposits accumulated in a salt minibasin offshore Espírito Santo Basin (SE Brazil). We identified three Miocene mass-transport deposits within the same stratigraphic interval, and four other in Holocene strata. Our interpretation reveals that the internal deformation of mass-transport deposits in the salt-withdrawal basin relates to their long-axis orientation. As a result, mass-transport deposits are divided in two types: a) Type 1 have the long axis parallel to the direction of movement and generally show significant internal deformation; b) Type 2 have their long axes perpendicular to the direction of movement, are highly heterogeneous and include large undeformed slabs. The long axes of Type 2 mass-transport deposits are also parallel to the strike of bounding elongated structures. The majority of mass-transport deposits are intensely deformed in their headwall regions. Relative short remobilisation distances are inferred for Types 1 and 2, with run-out distances being influenced by nearby salt structures and basin geometry. This study shows, for the study area, that the timing of emplacement of mass-transport deposits is associated with the growth of adjacent salt ridges. Earlier halokinesis in the northern axial areas of the minibasin shifted southwards in a second stage and triggered instability along the flanks of salt ridges. In addition, Holocene mass-transport deposits suggest alternating growth between the eastern and western salt ridges. Our results show that detailed seismic-stratigraphic analyses are key to understand the timings and magnitude of deformation of mass-transport deposits in salt minibasins. The classification here proposed is widely applicable to MTDs on continental margins worldwide and in lacustrine settings.

Keywords: Continental margins; salt diapirs; mass-transport deposits; salt minibasins; timing of halokinesis, Espírito Santo Basin.

1. Introduction

Mass-Transport Deposits (MTDs) reflect one of the key processes responsible for the shaping of the seafloor on active and passive continental margins, transferring large masses of sediment from proximal to distal slope domains (Hampton et al., 1996; Masson et al., 2006). Long-term trigger mechanisms for MTDs can relate to variable processes such as sediment loading, fluid overpressure, the presence of weak layers, or increasing slope gradients with time. Short-term triggers derive from processes such as earthquakes, tectonic oversteepening, gas seepage, hydrate dissociation, volcanic event, halokinesis or sea level changes (Lee, 2009; Masson et al., 2006; Posamentier and Martinsen, 2011; Sultan et al., 2004).

The emplacement of MTDs involves the remobilisation of material from a headwall region along a basal interval, documenting a

continuum of deformation styles along their transport direction(s) (Alves and Lourenço, 2010; Bull et al., 2009; Butler and McCaffrey, 2010; Tripsanas et al., 2008). As a result, extensional structures are often observed near the headwall and change downslope into a transitional domain with increasing strata disaggregation (Bull et al., 2009). This morphology culminates in a compressional toe domain that is often characterised by thrusting and folding of strata, or in the complete disaggregation of the remobilised material (Frey-Martinez et al., 2005). Brittle and ductile deformation occurs progressively within MTDs, depending on controls such as strata cohesion and run-out distance (Bull et al., 2009; Masson et al., 2006; Posamentier and Martinsen, 2011). Thus, MTDs can be highly heterogeneous, comprising variable proportions of blocks, slump folds and a disaggregated debris matrix. Blocks consist of semi-preserved strata that are named as: a) rafted if remobilised to any degree within or beyond the toe of the MTD, or b) remnant if they are kept *in situ* and represent isolated volumes of strata in vertical stratigraphic continuity with underlying non-MTD units (Alves, 2015; Bull et al., 2009; Frey-Martinez et al., 2005). Rafted blocks comprise a spectrum of morphologies, in which slide slabs are included. These latter form tabular masses of hundreds to thousands of metres in length and tens of metres in height, thus having very low thickness-to-length ratios (O'Leary, 1991; Varnes, 1978).

The proliferation of 3D seismic data has led analyses of the internal complexity of MTDs and their remobilisation dynamics along large areas of continental slopes (Bull et al., 2009; Gee et al., 2006; Omosanya and Alves, 2013b). Such a plethora of information resulted firstly in classifications of MTDs based on their frontal geometries. They classify as frontally confined slides when fully buttressed against a frontal ramp or frontally emergent where the remobilised mass is able to ramp-up the frontal confinement (Frey-Martínez et al., 2006). The interpretation of large datasets also allowed the classification of MTDs into slope- or shelf-attached systems, or locally detached systems where the mass-failure deposits do not link to the proximal domain (Moscardelli and Wood, 2008).

Salt upwelling and withdrawal closely control mass-transport deposits on salt-rich continental margins, and are key drivers of slope deformation (Giles and Rowan, 2012; Jackson et al., 1994). In this setting, strata deposited over growing salt structures are either thinned or completely removed by erosional processes, and can accumulate as MTDs in peripheral salt-withdrawal basins (Gamboa et al., 2011; Giles and Lawton, 2002; Tripsanas et al., 2004). Detached MTDs thus predominate over far-reaching slope-attached MTDs in distal minibasins of the Gulf of Mexico, Brazil and West Africa, leading to the deposition of heterogeneous strata that can be tied to key periods of salt movement (Beaubouef and Abreu, 2010; Jackson, 2012; Madof et al., 2009; Olafiranye et al., 2013).

This paper investigates buried and modern MTDs occurring in salt minibasins on the continental slope of Espírito Santo, SE Brazil. It presents a detailed description of a) three buried MTDs within a common depth interval and b) four modern deposits on the sea floor. Here, we present detailed maps of the top and base surfaces of the studied MTDs, complemented with thickness and amplitude maps, variance slices and gradient profiles in order to assess their internal heterogeneity. In the discussion section are compared the characteristics and degree of

internal deformation of two distinct types of MTDs, and how they can be used as markers for short-term halokinesis.

2. Geological Setting

2.1 Espírito Santo Basin

The Espírito Santo Basin is the northernmost of a series of Mesozoic rift basins located on the southeastern Brazilian margin (Fig. 1) (Davison, 2007; Fiduk et al., 2004). After the rift and transitional stages, the latter of which records the deposition of thick evaporitic units within a restricted basin, a two-phase drift stage dominated the Late Cretaceous to Cenozoic evolution of SE Brazil (Figs. 1c and 2) (Fiduk et al., 2004; Mohriak, 2003). During the Albian, a shallow-water carbonate platform accumulated underneath Late Cretaceous-Paleocene mudstones due to relative deepening of the Espírito Santo Basin in the early drift stage. The transition to the late drift stage (Lower Eocene) records the onset of a marine regressive megasequence, which takes the form of a thick prograding sequence on the continental slope (Davison, 2007; Demercian et al., 1993; Mohriak, 2003; Moreira and Carminatti, 2004).

Several erosive episodes took place in the Espírito Santo Basin during the drift phase, and resulted in the development of eleven (11) unconformities associated with major episodes of submarine channel incision on the proximal domains of the basin (Fiduk et al., 2004; França et al., 2007) (Fig. 1c). In parallel, recurrent Eocene-Miocene mass-wasting events led to the deposition of thick and laterally continuous MTDs in proximal and mid-slope parts of Espírito Santo (Fig. 2) (Gamboa et al., 2010; Omosanya and Alves, 2013a).

Thin-skinned extension of Cenozoic strata above Aptian evaporites led to development of an array of salt-related structures across the margin (Fig. 2). Extensional structures occur in proximal areas characterised by thin salt, and are followed by a wide area of salt diapirs in the mid-slope transitional domain (Fig. 2). Allochthonous salt walls and canopies occur in the more distal compressional domain (Davison, 2007; Demercian et al., 1993; Fiduk et al., 2004; Mohriak, 1995). Recent salt growth episodes also led to marked deformation of the modern seafloor (Fiduk et al., 2004) (Fig. 1b and 2).

Salt tectonics has a close relationship with the sedimentary evolution of the Espírito Santo Basin. Not only is the Late Cenozoic peak in halokinesis related to an increase in sediment input to the continental slope, but salt structures also exert a major control on the geometry of the sedimentary pathways and associated deposits across the slope (Fiduk et al., 2004; Love et al., 2005)

2.2. Local geological setting

The region interpreted in this paper is located on the distal domain of the Espírito Santo Basin, where salt-withdrawal minibasins develop due to the growth of allochthonous salt structures (Fig. 1 and 2). The minibasin investigated here follows a N-S orientation and is bounded by N-striking salt ridges (R1 and R2) respectively to the west and east (Fig. 1b and 3). Water depth ranges from 2000 m on the crest of R1 to 2330 m in the axis of the main minibasin.

Two main Cenozoic stratigraphic units are identified on 3D seismic data (Fig. 3). The shallower unit is interpreted to be Miocene to Holocene in age, and shows low to moderate amplitude seismic reflections with good

lateral continuity. Chaotic strata in this interval indicate the presence of MTDs (Fig. 3a and 3b). The deeper stratigraphic unit is Eocene to Oligocene in age, being characterised by moderate to high amplitude internal reflections. Reflection continuity is variable, and is often interrupted by MTDs with low to moderate amplitude, chaotic reflections (Fig. 3a). Detailed stratigraphic data is not available to tie the stratigraphic units to the 3D seismic volume. However, the seismic amplitude and relative abundance of MTDs suggest the interpreted units to be equivalent to those in the proximal domain of the Espírito Santo Basin (Gamboa et al., 2010).

Halokinesis, i.e. the ductile movement of buried evaporitic units (Jackson et al., 1994), induces important faulting in stratigraphic successions deposited in the minibasin (Fig. 3, 4b and 4c). However, fault distribution in the study area is not uniform and results from spatially variable interactions between the salt ridges and deeper structures (Fig. 3b). Hence, a high number of closely spaced faults are observed to the north, showing orientations sub-perpendicular to the salt ridges (Fig. 3c). Faults are scarcer towards the central and southern areas of the minibasin, and only observed close to the high-curvature segment of ridge R1 (Fig. 4c).

3. Data and Methods

The interpreted 3D seismic volume covers an area of ~276 km^2 on the distal continental slope of the Espírito Santo Basin (Fig. 1). Data acquisition used a dual airgun array and six 5700 m-long streamers. Seismic signal was sampled at 2 ms and zero-phased migrated with a 12.5 m grid line spacing (inline and crossline).

In addition to the seafloor, four continuous horizons (H1 to H4) where mapped within the minibasin (Fig. 3). Horizons H1 and H4 delimit the interval of occurrence of the buried MTDs interpreted in this work. Horizon H1 underlies the MTDs, below which the seismic reflections are relatively undisturbed. The top horizon is interpreted as the topmost seismic reflection presenting the style(s) of deformation associated with the deposit, i.e. the shape of the seafloor immediately after the emplacement of the mass-transport deposit (Bull et al., 2009; Masson et al., 2006). Seismic attributes of interest to our analysis included RMS (root-mean square) amplitude and variance slices. The variance slices in this paper were extracted from a volume flattened at H1 (Fig. 3), allowing for the assessment of the MTDs' internal geometry at equal time intervals above and below their basal surfaces (Fig. 4b and 4c).

In this paper, MTDs were characterised based on their morphometrics and relative thickness. We opted for parameters such as the length of 'long' and 'short axes' - instead of length and width - to characterise the dimensions of what is a series of elongated MTDs on map view. As a result, any reference to length or run-out distance(s) relate to a quantitative parameter with a sub-parallel orientation to the direction of transport of an MTD, with width being sub-perpendicular to this latter (Moernaut and De Batist, 2011; Moscardelli and Wood, 2015; Varnes, 1978).

To help our analysis, the 3D seismic volume was depth-converted within the intervals of interest using an estimated seismic velocity of 1500 m/s for the water column, and 1800 m/s for buried strata, based on velocity profiles at DSDP site 516 (Barker et al., 1983). The latter p-wave velocities and the dominant frequency of 40 Hz of the seismic volume indicate a vertical resolution of 19 m at the depth of the interpreted MTDs.

The horizontal resolution approaches 12.5 m, a value equivalent to the gridline spacing of the seismic volume.

4. Description of MTDs in the distal Espírito Santo Basin

Thickness maps were computed for the stratigraphic interval spanning H1 and H4 (Fig. 4a). Three MTDs, named MTD A, B and C, were interpreted within this same interval (Figs. 3 and 4). These deposits share a common base horizon along H1 (Fig. 3), and their occurrence led to localized strata thickening within the axis of the studied minibasin (Fig. 4a).

4.1. MTD A

MTD A occurs on the axis of the salt minibasin and is delimited by H1 and H3 (Fig. 5). It shows continuous internal reflections of moderate amplitude (Fig. 5a, 5b and 5c). MTD A shows a SW-trending long axis, sub-parallel to its run-out direction. Its long and short axes show values of 4772 m and 2900 m, respectively, and the deposit has a volume of 0.34 km^3 within an area of 13.3 km^2 (Fig. 6).

The base of MTD A (horizon H1) shows a stepped morphology associated with sets of WNW-trending faults (Fig. 5a and 6a). The steeper gradients in horizon H1 range between 7º and 17º over the faults, whereas the flatter areas do not exceed 2º (Fig. 6a). The top surface of MTD A (H3) mimics the morphology of H1, but presents smoother slope breaks and arcuate ridges (Figs. 5a, 5d and 6a). Its steeper part is located towards the north, associated with local erosional scarps (Fig. 6a). A sharp irregularity is observed on H3 over a small horst structure (Fig. 5a). MTD A comprises an extensional headwall domain to the north, with two main faults defining a headwall scarp with generally straight segments (Fig. 5a, 5d and 6c). Disaggregated facies extend northwards of the fault scarps, and indicate the presence of local retrogressive failures (Fig. 5a and 5d). The thinner MTD strata in the headwall domain reveal important remobilisation upslope (Fig. 6b).

Thickness data for MTD A shows a heterogeneous accumulation of sediment (Fig. 6b). The thicker accumulations reach ~45 m in the southeastern part of the toe domain. Other WNW-trending patches reach 30 m in the middle of MTD A (Fig. 6b). The thinner accumulations, between 8 m and 15 m, are adjacent to E-W headwall faults. Such variability in thickness reflects a marked zonation in MTD A, with well-delimited boundaries bounded by underlying faults (Fig. 5a).

Variance slices from MTD A indicate heterogeneous deformation in the form of arcuate ridges alternating with areas of low variance (Fig. 6c). In general, ridges with downslope-facing convexity mark the presence of compressional structures, whereas downslope-facing concave features are associated with extensional faults (Fig. 5a and 5b). In addition, compressional ridges show higher lateral continuity on attribute maps, whereas extensional faults show shorter segments (Fig. 6c). Root-Mean Square (RMS) amplitude maps further highlight this internal heterogeneity by showing the arcuate ridges as alternations of high and low amplitude reflections coincident with areas of changing variance (Fig. 6d). As these deformation features are associated with thickness variations in MTD A, we interpret that marked variations in strata remobilization occur in distinct sections of the deposit. Thus, localised compression at the centre of MTD A is

followed downslope by an extensional domain with numerous normal faults, akin to a secondary headwall region (Fig. 5a, 5b, 6c). This transitions into the toe domain of MTD A, where two sets of compressional ridges are identified: a) a main set with SSW-facing convexity in strata 20 to 35 m thick, and b) a secondary set located on the southwest part of MTD A (Figs 5d, 6b and 6c). Ridges in this latter region verge to the west, showing higher curvature and shorter spacing (Fig. 6c and 6d). Overall, kinematic indicators in MTD A show the bulk of the movement to follow a SSW direction, but with variable confinement at the toe being controlled by pre-existing faults **(**Fig. 5d). This character results on a progressively emergent front with a 50º westward shift of the flow due to a decrease in fault throw (Figs.5d and 6c).

4.2. MTD B

In the study area, MTD B is delimited by horizons H1 and H4 at its base and top (Fig. 7a). It shows an identical value of ~2500 m for its long and short axis, covering an area of 6.4 km^2 for a calculated volume of 0.4 km^3. The source area of MTD B is located on the SW flank of salt ridge R2 (Figs. 7a and 7d), and the deposit thickens towards its toe area to a maximum of 80 m. In addition, localised thickening is observed on a 350 m-wide erosional slot located upslope (Fig. 7a and 7c). Slope gradients of the basal horizon H1 reach 8º over the steeper flank of the salt ridge, but decrease to 1.3º towards the west (Fig. 6a). Locally, H1 shows multiple steps dipping towards the ridge flank, which are coincident with the frontal ramp of the erosive slot (Fig. 7a). The lack of a sharp headwall scarp in MTD B is likely a result of post-failure halokinesis.

A seismic profile along the long axis of MTD B shows low amplitude and disrupted reflections near its upslope termination (Fig. 7a). However, variance slices reveal crescent-shaped features (which are associated with extensional faults) within the general mottled character of the headwall area (Fig. 7d). Reflection continuity increases downslope, becoming identical to non-remobilised strata at the toe of the MTD (Fig. 7a). Elongated ridges cross the full width of MTD B, and show a regular spacing of 50 m to 60 m (Fig. 7d and 7e). The ridges record compression at the front of MTD B, as they are associated with imbricated west-facing internal thrust faults (Fig. 7a). The frontal ramp of MTD B is not bounded by any major fault (Fig. 7a).

4.3. MTD C

MTD C occurs on the flank of salt ridge R1 (Figs. 8 and 9). Its NE-SW long axis reaches 11100 m, and is subparallel to the orientation of ridge R1 (Fig. 9a). Its short axis measures ~4500 m for a volume of remobilised material reaches 2.60 km^3 i.e., 6 to 8 times larger than MTDs A and B. MTD C covers an area of 41 km^2. Importantly, the orientation of its long axis is sub-perpendicular to its run-out direction (Fig. 8 and 9).

The thickness of MTD C increases eastwards, with the thinnest strata occurring along its headwall area (Fig. 9c). The thickest accumulations range between 70 m and 90 m along an elongated toe area near the axis of the mini-basin. Large portions of strata in the middle domain of the MTD show a uniform thickness (Fig. 8 and 9a). This is due to the presence of slabs *sensu* O'Leary (1991) of well-preserved strata in MTD C. These slabs are flat and relatively thin (around 60 to 70 m) when compared to their length and width,

which always exceed 1000 m. Due to their minor internal deformation, the slabs show low variance (Fig. 9d) and good reflection continuity, identical to non-remobilised strata in other parts of the slope (Figs. 8 and 9d**).**

Variations in slope gradients at H1 and H4 are associated with changes in the heterogeneity of MTD C. Extensional domains upslope show a general gradient of 3.7º along H1, but local features can reach 15º to 20º (Fig. 9b). At mid-MTD locations, the basal interval underneath the rafted slabs shows slope gradients of ~3º, decreasing downslope to approximately 1º. The top of MTD C shows gradients of 3º upslope, and is marked by irregularities associated with sediment remobilisation. The top of the slabs shows smooth surfaces dipping 2º to 2.5º, followed downslope by gradients <1º where the compressional ridges are observed (Fig. 9b).

The complex morphology of the top of MTD C (H4) highlights three different domains. Rugged patterns are observed in the headwall and toe areas due to internal folding and faulting during sediment remobilisation (Fig. 8b, 8c, 9a). Crescent-shaped faults, possibly associated with regressive slope failures (Galloway, 1998), occur adjacent to longer linear faults in the headwall domain.

Within the upslope domain, closely spaced extensional faults are present near the inferred scarps (e.g. Fig. 8c) while thrust faults can develop towards the east, adjacently to the western flanks of the MTD slabs (Fig. 8b). Elongated ridges spaced between 90 m and 100 m are observed in the toe domain, eastwards of the slabs (Fig. 8b, 8d, 9d, 9e). Significantly, the toe ridges are bound by east- and west-dipping faults, with continuous seismic reflections occurring within the fault-bound blocks (Fig. 8b and 8d). These compressional structures define a series of wedge-shaped pop-up blocks of cohesive strata along the toe of MTD C, which contrasts with the disaggregated facies and imbricated toe thrusts of published MTD models (e.g. Frey-Martinez et al., 2005). The majority of the compressional ridges are oriented N-S, but sub-perpendicular W-E segments of limited extent are also observed (Fig. 9d).

Based on local kinematic indicators, MTD C records eastward movement along the steeper flanks of salt ridge R1 and strata was remobilised as far as the low-gradient axis of the salt minibasin (Fig. 4a). The salt ridge and associated faults play a role in the delimitation of the MTD headwall (Fig. 8 and 9d). However, the presence of scalloped scarps suggest the presence of a complex headwall and the occurrence of localised retrogressive failure events in areas not strictly delimited by faults related to the salt structures (Fig. 8b and 9d).

4.4. Seafloor MTDs

Several seafloor MTDs are observed in the study area (Fig. 10 and 11). The roughness of the seafloor maps shows the great majority of modern MTDs to be adjacent to structural highs created by salt ridges, and over the locations of MTDs B and C. In addition, small failure events and arcuate fractures are observed over MTD A in the axial areas of the salt minibasin (Fig. 1b). Four seafloor MTDs are described in this section (SF1 to SF4) in order to compare their morphology to the buried MTDs A to C.

MTD SF1 occurs on the western flank of ridge R1 (Fig. 10b). It shows a long axis of 2380 m, striking parallel to the salt ridge, and a short axis of 1280 m parallel to the run-out direction (Fig. 10a and 10c). Remobilised strata in its upslope domain range between 32 and 45 m in thickness, and are delimited to the east by a scalloped headwall with

extensional faults (Fig. 10a, 10c and 10d). Two elongated rotated blocks up to 60 m thick and ~500 m long, showing very moderate remobilisation, occur close to the headwall (Fig. 10a). Elongated slabs parallel to the long axis of SF1 are present in the mid-MTD domain, showing smooth top surfaces and a relatively uniform thickness of 45 m (Fig. 10a and 10d). The toe domain of the deposit is up to 59 m thick, where elongated compressional ridges develop along the full width of SF1 (Fig. 10d). These characteristics are in all identical to the morphology of MTD C, mirroring the downslope relationship between rugosity and gradient changes of the MTDs bounding surfaces (Fig. 10c).

MTD SF2 is located on the eastern flank of ridge R1, being 4550 m long and 1930 m wide (Fig. 10b). The long axis of SF2 is oriented towards the SE, sub-perpendicular to the salt ridge. Within the bulk of SF2, strata in the extensional domain reaches a thickness of 20 m to 35 m, confined by a frontal ramp. In its compressional domain, the thickness of SF2 can reach 85 m in areas of imbricated thrusting (Fig. 10b, 10e and 10f). Furthermore, an elongated thin deposit with up to 25 m in thickness is observed at the front of SF2 (Fig. 10b and 10e), resulting from an emergent flow that extends 2400 m beyond the bulk of SF2. These morphological trends are identical to MTDs A and B (Figs. 4 and 5).

MTD SF3 is located on the flank of ridge R1, ~1800 m southwest of SF2 (Fig. 10b). It is 3140 m and 1520 m along its long and short axes, respectively, being delimited upslope by a concave headwall scarp (Fig. 10b and 10g). Two locations with strata pinch-outs, where thickness does not exceed 25 m, occur in the evacuation area adjacent to the scarp. This is followed downslope by strata ~65 m thick located 1200 m away from the headwall scarps (Fig. 10h). An elongated deposit, up to 25 m in thickness, extends ~2000 m further downslope along a 200 m and 500 m-wide area beyond the main SF3 body (Fig. 10g and 10h). Seismic profiles show characteristic mottled reflections within the main body of SF3. However, elongate deposits from the emergent front are represented by continuous reflections with subtle irregularities and amplitude variations. These small lateral modifications in reflection character support the interpretation of thin remobilised strata in SF3, despite its similar aspect to intact strata nearby (Fig. 8g).

MTD SF4 is located along ridge R2 and reached a run-out of 2000 m to 2500 m (Fig. 11). Although the overall long axis of the deposit is parallel to the strike of R2, discrete flows oriented perpendicularly to the ridge are interpreted to form SF4. A complex headwall scarp bounds SF4 to the east and to the north, along the ridge flank. The scarp limit is identified at depths of ~2100 m, although steeper scarps occur higher on the ridge at depths of 2045 m (Fig. 11a). A remarkable feature of discrete slope failures occurring along ridge R2 is the general lack of chaotic reflections below the seafloor (Fig. 11b). Instead, evidence of strata deformation associated with SF4 is expressed by small-scale irregularities along single continuous reflections, similarly to the character of turbiditic or drape deposits (Fig. 11b). Thus, SF4 shows a relatively smooth top surface with limited relief on the seafloor. This can result from post-depositional reworking and sediment drape. However, the moderate subsurface deformation observed on seismic also suggests that SF4 is associated with relatively thin, low volume flows with limited morphological expression on the seafloor (Fig. 11b).

5. Quantitative analysis of MTDs

Quantitative analyses show that the buried MTDs A to C, located between H1 and H4, are the largest in the study area. They show long axes values between 3000 m and 12000 m and short axes between 2500 and 4500 m. By comparison, sea-floor MTDs are smaller, not exceeding 3150 m and of 2000 m in their long and short axes (Fig. 12). Nevertheless, long/short axes ratios for all interpreted MTDs show similar ranges, regardless of their orientation, size and stratigraphic position (Fig. 12a). The lower values were recorded for MTD B, with long/short axes ratios near one.

Comparisons between the area and volume of all MTDs indicate similar scale-relationships, despite their difference in size (Fig. 12c). Positive correlations were also observed between the area and volume of the slabs in MTD C (Fig. 12d), most likely due to the uniform thickness recorded. The size of the large slabs in MTD C is also similar to the ranges of length and width values of individual large mass-transport blocks identified on slope-attached MTDs on the proximal Espírito Santo Basin (Fig. 12e). This suggests that similar dimensional ranges can occur both in the proximal and distal domains of continental margin for distinct MTDs (see also Alves and Cartwright, 2009; Gamboa and Alves, 2015).

The headwall length of the interpreted MTDs show a good correlation with both the area and volume of the interpreted deposits (Fig. 12f and 12g). Bar the larger deposit (MTD C), all data points in the headwall length-area plot fall close to the fitted trend line, for a correlation coefficient of 0.9 (Fig. 12f). Similarly, MTD volume also show a positive correlations with headwall length, with a correlation coefficient of 0.85 (Fig. 12g). A ratio between headwall length and its distance to the toe of the MTDs was also calculated (Fig. 12h). The results show values above one for MTDs C and SF1, which have long axes perpendicular to their run-out direction (Fig. 9 and 10a), whereas the majority show ratios below one. The values and trends observed indicate a close relationship between the geometry of the interpreted MTDs. However, care must be taken when analysing their relationships as the short number of samples (MTDs) used may compromise their statistical significance.

6. Discussion

6.1. Bi-modal MTD types in confined minibasins

The majority of MTDs in the study area show elongate morphologies typical of remobilised slope strata, regardless of their location within the salt minibasin (Figs 1 and 3). Apart from their overall size, in which buried MTDs are clearly larger (Fig. 12b), there is no clear difference in the long/short axes ratios values between buried and seafloor MTDs (Fig. 12a). Importantly, long/short axes ratios of MTDs do show any relationship with the observed variability in internal deformation (Figs. 3, 5, 8 and 10). The MTDs in the salt minibasin show close relationships between their area and volume (Fig. 12c). These two parameters also correlate well with the length of the headwall area (Figs. 12f and 12g), similarly to trends observed in Klar et al. (2011), Micallef et al. (2008) or Moernaut and De Batist (2011).

A clear distinction between MTDs is observed when comparing the length of the

headwall area to the measured distance-to-toe (Fig. 12h), which in this study can be considered equivalent to their length. The results show a bi-modal trend in the MTDs' headwall length/distance-to-toe ratios (Fig. 12h). Several deposits show ratios below or close to one. However, MTDs C and SF2 show significantly higher values (Fig. 12h). These differences are linked to the orientation of the long axes of the two MTDs when compared to their run-out direction, and internal heterogeneities. Such contrasts are observed by comparing, for example, MTDs A and C (Figs. 3a, 5d and 9d).

Based on this, we define two types of MTDs – Type 1 and Type 2 - according to their morphology. Type 1 MTDs are characterised by headwall length/distance-to-toe ratios below one (1), meaning that the long axis of the deposit is sub-parallel to its length and the direction of movement (Fig. 13a).

Type 2 MTDs are likely to be comparatively less common, being characterised by a long axis orientation sub-perpendicular to their length and direction of movement. Type 2 MTDs show headwall length/run-out distance ratios above one. Type 2 MTDs are represented in the study area by MTDs C and SF1, showing very similar internal characters i.e., presenting slabs in a generally convergent, frontally confined flow. Other published examples of Type 2 MTDs have been observed adjacent to salt ridges in West Africa (Maia et al., 2015), in the Gulf of Mexico (Posamentier and Martinsen, 2011; Madof et al., 2009), and in lacustrine settings (Moernaut and de Batist, 2011).

The definition of the type of deposit must take into account not only their geomorphic trends but also the evolutionary relationship between the components that form the deposit. In the study area, MTD SF4 can be used to exemplify this relationship. Despite showing (large) headwall length/run-out distance ratios characteristic of Type 2, SF4 is composed of multiple (and likely diachronous) ridge-perpendicular Type 1 flows along ridge R2 (Fig. 11). Type 1 MTDs could also have similar geometry to Type 2 in flows diverted and entrenched along the axis of narrow confined basins. Identifying the length of the source area and comparing it to the MTD run-out is therefore key to distinguish both types of MTDs.

6.2. Internal deformation in Types 1 and 2 MTDs

Deformation styles in complex MTDs show a wide range of structures associated with variable degrees of strata disaggregation, flow velocity, flow orientation, and remobilisation distances (Ashabranner et al., 2010; Gamboa et al., 2011). In general, there is a direct correlation between the degree of strata disaggregation, remobilisation distance and flow velocity (Posamentier and Martinsen, 2011; Nemec, 1991). Thus, the lower the flow velocity, the higher the potential to preserve intact remobilised strata. Although the classic slope instability models tend to show an increasing deformation continuum from the headwall to toe area (Bull et al., 2009), such models are not fully applicable to some of the complex MTDs interpreted in this work, especially when deformation decreases along their run-out distance.

6.2.1. Type 1

Type 1 MTDs tend to have higher degrees of internal deformation and develop frontal domains with numerous imbricated thrusts and ridges (Fig. 13a), as exemplified by MTDs A, B, SF2 and SF3 (Figs. 5, 7 and 10).

Their thickness thins upslope in extensional domains and thickens in compressional areas, regardless of their relative position within the MTD. Frontal confinement is common in Type 1 MTDs, but thinned emergent sections of the flow can also occur (Fig. 13a). This variability in frontal confinement can be influenced by structures underlying the MTDs, as exemplified in MTD A (Fig. 5). Frontal ramps confined MTD A where the highest fault throws were sufficient to dissipate the flow energy (Fig. 5b), but the smaller fault offsets observed in its southwestern sector allowed the flow to emerge and run for 850 m beyond the main frontal fault (Fig. 5d). However, Type 1 MTDs not controlled by faults can have significantly longer emergent fronts, as exemplified in the study area by the seafloor MTDs (Fig. 11). The preferential occurrence of contractional faults and ridges at the lower gradient regions along the MTDs' basal intervals (Figs. 6a and 13a) suggests dissipation of kinetic energy induced by a structurally-controlled decrease in slope gradient - ultimately favouring the arrest and frontal confinement of the flow (Frey-Martínez et al., 2006; Moernaut and De Batist, 2011). Secondary extensional and contractional domains also occur, as exemplified at the middle part of MTD A, where internal deformation styles are associated with gradient variations along the stepped basal interval (Figs. 6a and 13a). The basal structures force the buttressing and thickening of strata at the upslope flank of MTD A, followed by extension and possibly flow acceleration at its downslope flank, similarly to structurally influenced deformation in the Tampen Slide (Gafeira et al., 2010).

6.2.2. Type 2

Type 2 MTDs are exemplified by MTDs C and SF1, which show marked contrasts in deformation (Figs. 9, 10a and 13b). A common aspect of both MTDs is the presence of slabs of uniform thickness at their translational domains. These slabs separate upslope evacuation domains from the long compressional ridges at the toe of the MTDs (Figs. 8, 9d and 13b). A striking aspect of these slabs is their size and (intact) aspect on the seismic data, particularly in MTD C (Figs. 8 and 9). They show an (apparent) vertical continuity with underlying *in situ* strata, a property more commonly associated with remnant blocks (Alves, 2015; Bull et al., 2009; Gamboa et al., 2011). Intra-slab shearing processes are also rarely identifiable on 3D seismic data, with slabs considered to have moved as 'frozen' masses. However, small intra-slab thrusts in MTD C, detaching at the base of horizon H3 (Fig. 8e and 13b), may represent internal bed-parallel shearing (Gamboa and Alves, 2015). This phenomena is also prone to occur in slabs sharing similar seismic characters, even when the deformation is not fully resolvable on seismic data. There is the possibility that MTDs C and SF1 represent an extreme case of internal strata preservation, and increased faulting and/or strata disaggregation can occur in the translational domains of more dynamic Type 2 MTDs. However, deformation in translational domains can still be generally lower when compared to the MTD headwall and toe domains, as observed in West Africa (Maia et al., 2015) or the Gulf of Mexico (Posamentier and Martinsen, 2011).

The increased deformation on the upslope sections of Type 2 MTDs is likely to be related to the higher slope gradients of the ridge flank, which induce higher flow velocities in the evacuation area and favour strata disaggregation. Considering a

simultaneous movement of all elements in Type 2 MTDs, contrasts in internal remobilisation velocity can develop secondary compression zones between the evacuation and translation domains, resultant from the buttressing of the faster headwall strata against the adjacent slow-moving slabs (Fig. 13b). In addition, recurrent failure events near the headwall also have the potential to increase the kinetic energy of remobilised masses and aid the movement of the large slabs (Kvalstad et al., 2005, Ogata et al., 2014) or, otherwise, further enhance upslope butressing structures if the slabs have stopped moving. Localised ridges sub-parallel to the direction of movement were observed in Type 2 MTDs, suggesting that secondary internal stresses orientations were generated during strata remobilisation (Fig. 6f, 7b and 13b). These stresses can be influenced by underlying faults, as in MTD C (Fig. 6a), or due to the deformation of softer strata confined between moving slabs. The long ridges at the toe result from a generally uniform compression controlled by the slow movement of slabs (Fig. 6f). While the upslope strata of Type 2 MTDs could have had variable remobilisation distances, at the central and toe domains of the deposit the remobilisation distance is considered to be comparatively lower, and reflecting slower flow velocities due to the high degree of strata preservation (Posamentier and Martinsen, 2011). Slab movement in MTD C was in the order of 50 m to 70 m, as estimated from the restauration of pop-up blocks at its toe to their original geometries. Such short remobilisations and the presence of pop-up blocks – which contrast with the imbricated toe thrusts of faster flows – suggest a low rate, progressive compression at the toe of MTD C induced by the slow movement of the slabs (Fig. 13b).

6.2.3. Factors influencing Type 1 and Type 2 MTDs

Local triggers of slope failure can be varied, consisting of tectonic movements, the presence of weak overpressured shales or gas hydrate dissociation, to name a few (Hampton et al., 1996; Masson et al., 2006; Posamentier and Martinsen, 2011). These are likely to generate either Type 1 or 2 MTDs, as both types occur in stratigraphic units of fairly uniform seismic character in the studied minibasin. Furthermore, the deposits studied here are likely to have identical trigger mechanisms and low remobilisation distances due to local structural controls on the flows. Short remobilisation distances can also supported by the predominant constrain of the studied MTDs to a flank or specific location within the salt-withdrawal basin, contrasting with highly remobilised deposits that pond at the centre of the minibasins (Madof et al., 2009).

The main factor leading to Type 1 or Type 2 MTDs is the length of the headwall area, as demonstrated by the morphological analysis undertaken in this work (Fig. 12). Additionally, variations in slope gradient, and possibly the volume of material prone to failure will also play a role in the development and deformation of the two types of MTDs. The slope gradient is consistently higher in evacuation areas of Type 1 MTDs, which can induce higher flow velocities (Posamentier and Martinsen, 2011) and explain the higher deformation observed (Figs. 5 and 10b). The moderate deformation and length of Type 2 deposits could hypothetically relate to lateral dispersion of the slope failure-inducing stress along a wider area and favour slower, more constrained remobilisations.

This classification is widely applicable to MTDs in other settings. Based on the data in

this work, Type 1 is likely to be the most common on the world's continental margins, fitting both large slope-attached elongate MTDs on continental margins and detached MTDs as seen here. Type 1 MTDs may tend to develop quite divergent flow patterns if largely unconfined, particularly in very large MTDs in open slopes. In contrast, Type 2 MTDs are less common and prone to prevail in confined basins bound by elongate unstable structures such as salt ridges. These may tend to relatively limited run-out distances, and convergent (this work) or divergent flow patterns (e.g. Posamentier and Martinsen, 2011), depending on the curvature of the flanking structure.

6.2. Timing of MTDs as indicators of salt deformation

Multiple slope failures in salt-withdrawal basins can be associated with specific pulses of salt growth or withdrawal subsidence, and the MTD horizons used as time markers for regional deformation episodes (Madof et al., 2009). However, large magnitude failures are only likely to relate their base interval to a major pulse of salt deformation, thus not being able to record subtler deformation episodes occurring along the basin during a restricted time interval.

As the buried Miocene MTDs share the same detachment surface (Fig. 3), it is possible to estimate a relative chronology and spatial order of salt-influenced slope failures within a restricted time interval in the minibasin. MTD A is the oldest mass-failure occurring along H1 as its top is delimited by horizon H3, while the remaining MTDs are capped by H4 (Fig. 14a). This suggests that during the time interval between the deposition of H3 and H4 relevant, and possibly fast halokinetic deformation, occurred in northern part of the salt minibasin. Such phenomenon could have had the potential to reactivate the large faults underlying MTD A (Fig. 5), inducing localised subsidence and triggering an MTD at an uncommon location on the axis of the minibasin (Fig. 14a). Post-MTD tectonic pulses, if occurring, were less intense as no large remobilisation indicators occur where horizon H4 overlies MTD A (Fig. 14a). However, some degree of instability is likely to have occurred through time within this area, as shown by the cracks and minor slides on the modern seafloor (Fig. 3b and 14a). Subsequent tectonic instability of the salt structures likely occurred at the southern areas of the minibasin, as indicated by MTDs B and C that occurred during the time in which H4 constituted the paleo-seafloor (Fig. 14a). Finding the time relationships between these MTDs can indicate if they occurred at the same time due to a major subsidence of the southern area of the basin or if due to diachronous movements between ridges R1 and R2. However, this is a difficult task to achieve on seismic data alone as there is a lack of evident cross-cutting relationships between these MTDs, or any unambiguous interference between their toe structures (Fig. 4b, and 9d). The flank-derived MTDs are most probably separated by a short time period, but in such a context MTD C is likely to materialise a larger duration of the remobilisation event due to its size and the presence of large slow-moving slabs.

Assessing the relative timings of emplacement for the modern MTDs is also difficult as there are no clear intersections between the different deposits due to their limited run-out distances (Fig. 1b, 10, 11 and 14b). However, the morphology of the seafloor MTDs can be used as a proxy to interpret their relative age as sharper scarps and edges often indicate younger deposits

less smoothed by erosion or draping (Tripsanas et al., 2004). The higher smoothness of the MTDs flanking ridge R2 indicates these are older than the majority of slope failures identified along R1 (Fig. 14b). However, based on scarp sharpness there are also recent failure events derived from scarps at shallow depths, closer to the crest of R2 (Figs. 9). Overall, we hypothesise that on recent times there was relevant salt-induced deformation, with major instability episodes initially taking place along ridge R2 and subsequently on the flanks of ridge R1 (Fig. 14b).

7. Conclusions

This paper proposes a classification of two types of MTDs, Type 1 and Type 2, based on the quantification of headwall length/distance-to-toe ratios measured for seven distinct MTDs:

a) Type 1 MTDs are defined by headwall length/distance-to-tore ratios below one (1), having their long axis parallel to the direction of movement.

b) Type 2 MTDs show headwall length/distance-to-tore ratios above one (1) and a long axis perpendicular to the runout direction.

c) The deformation styles of MTDs correlate with their types. Type 1 MTDs show intense, but less complex deformation with thinned evacuation domains followed by thickened toe domains with compressional ridges and variable frontal confinement. Type 2 MTDs show marked lateral changes of internal deformation styles.

Of relevance is also the enhanced strata preservation observed at the transitional domains of Type 2 MTDs, represented by slabs of coherent strata, when compared to the higher disaggregation at source regions. Secondary compressional and extensional domains have been identified in both Type 1 and Type 2 MTDs. The presence of underlying structures, or a combination of variable slope gradients and internal MTD flow velocities, can induce the genesis of these secondary deformation domains.

This work also highlights how MTDs can be used to locate shifts of salt-related instability areas through time. Buried MTDs suggest that salt movement was initially located on the northern part of the studied salt minibasin. Subsequent halokinetic pulses occurred southwards and caused the slope failures on the salt ridges. The morphology of seafloor MTDs is also used to relatively date periods of slope instability on distinct salt ridges.

The MTD classification in this work are applicable to marine and lacustrine settings worldwide, and can be used to predict the deformation character and remobilisation dynamics of these deposits. This is particularly the case for the less common Type 2 MTDs, whose geometry puts in question the deformation models established for slope failures. The examples of the slabs shown in this work highlight the important of the correct identification of remobilised strata on continental margins. If merely based on individual seismic profiles the rafted slabs can be misinterpreted as unremobilised strata when relevant slope movement and deformation has occurred.

7. Acknowledgements

The authors thank CGG for the permission to publish the data presented in this paper. Schlumberger is acknowledged for the provision of seismic interpretation software. The Sêr Cymru National Research Network for Low Carbon, Energy and Environment (NRN-LCEE) is acknowledged for partial funding that supported this research. Davide Gamboa publishes with the permission of the Executive Director, British Geological Survey. Joana Gafeira is acknowledged for the comments and discussions on earlier versions of this manuscript. We would also like to thank Joshu Mountjoy and an anonymous reviewer for their constructive comments, and Michele Rebesco for the editorial handling of the manuscript.

8. References

Alves, T.M., 2015. Submarine slide blocks and associated soft-sediment deformation in deep-water basins: A review. Marine and Petroleum Geology, 67: 262-285.

Alves, T.M. and Cartwright, J.A., 2009. Volume balance of a submarine landslide in the Espírito Santo Basin, offshore Brazil: Quantifying seafloor erosion, sediment accumulation and depletion. Earth and Planetary Science Letters, 288(3-4): 572-580.

Alves, T.M. and Lourenço, S.D.N., 2010. Geomorphologic features related to gravitational collapse: Submarine landsliding to lateral spreading on a Late Miocene-Quaternary slope (SE Crete, eastern Mediterranean). Geomorphology, 123(1-2): 13-33.

Ashabranner, L.B., Tripsanas, E.K. and Shipp, R.C., 2010. Multi-direction flow in a Mass-Transport Deposit, Santos Basin, offshore Brazil. In: D.C. Mosher et al. (Eds.), Submarine Mass Movements and Their Consequences. Springer, pp. 247-255.

Barker, P.F., Buffler, R.T. and Gambôa, L.A., 1983. A seismic reflection study of the Rio Grande Rise. In: P.F. Barker, R.L. Carlson and D.A. Hohnson (Eds.), Initial Reports of the Deep Sea Drilling Program, Washington, D.C., Government Printing Office, pp. 953-976.

Beaubouef, R.T. and Abreu, V., 2010. MTCs of the Brazos-Trinity Slope System; Thoughts on the Sequence Stratigraphy of MTCs and Their Possible Roles in Shaping Hydrocarbon Traps. In: D.C. Mosher et al. (Eds.), Submarine Mass Movements and Their Consequences. Springer, pp. 475-490.

Bull, S., Cartwright, J. and Huuse, M., 2009. A review of kinematic indicators from mass-transport complexes using 3D seismic data. Marine and Petroleum Geology, 26(7): 1132-1151.

Butler, R.W.H. and McCaffrey, W.D., 2010. Structural evolution and sediment entrainment in mass-transport complexes: outcrop studies from Italy. Journal of the Geological Society, 167(3): 617-631.

Davison, I., 2007. Geology and tectonics of the South Atlantic Brazilian salt basins. In: A.C. Ries, R.W.H. Butler and R.H. Graham (Eds.), Deformation of the Continental Crust: The Legacy of Mike Coward. Geological Society London, Special Publications 272, pp. 345-359.

Davison, I., Alsop, G.I., Evans, N.G. and Safaricz, M., 2000. Overburden deformation patterns and mechanisms of salt diapir penetration in the Central Graben, North Sea. Marine and Petroleum Geology, 17(5): 601-618.

Demercian, S., Szatmari, P. and Cobbold, P.R., 1993. Style and pattern of salt diapirs due to thin-skinned gravitational gliding, Campos and Santos basins, offshore Brazil. Tectonophysics, 228(3-4): 393-433.

Fiduk, J.C., Brush, E.R., Anderson, L.E., Gibbs, P.B. and Rowan, M.G., 2004. Salt deformation, magmatism, and hydrocarbon prospectivity in the Espirito Santo Basin, offshore Brazil. In: P.J. Post et al. (Eds.), Salt-sediment interactions and hydrocarbon prospectivity: Concepts, applications, and case studies for the 21st century. GCSSEPM 24th Annual Research Conference, pp. 370-392.

França, R.L., Del Rey, A.C., Tagliari, C.V., Brandão, J.R. and Fontanelli, P.R., 2007. Bacia de Espírito Santo. Boletim de Geociências da Petrobras, 15(2): 501-509.

Frey-Martinez, J., Cartwright, J. and Hall, B., 2005. 3D seismic interpretation of slump complexes: examples from the continental margin of Israel. Basin Research, 17(1): 83-108.

Frey-Martínez, J., Cartwright, J. and James, D., 2006. Frontally confined versus frontally emergent submarine landslides: A 3D seismic characterisation. Marine and Petroleum Geology, 23(5): 585-604.

Gafeira, J., Long, D., Scrutton, R. and Evans, D., 2010. 3D seismic evidence of internal structure within Tampen Slide deposits on the North Sea Fan: are chaotic deposits that chaotic? Journal of the Geological Society, 167(3): 605-616.

Galloway, W.E., 1998. Siliciclastic slope and base-of-slope depositional systems: component facies, stratigraphic architecture, and classification. AAPG bulletin, 82(4): 569-595.

Gamboa, D., Alves, T. and Cartwright, J., 2011. Distribution and characterization of failed (mega) blocks along salt ridges, southeast Brazil: Implications for vertical fluid flow on continental margins. Journal of Geophysical Research, 116(B8): B08103.

Gamboa, D., Alves, T., Cartwright, J. and Terrinha, P., 2010. MTD distribution on a 'passive' continental margin: The Espírito Santo Basin (SE Brazil) during the Palaeogene. Marine and Petroleum Geology, 27(7): 1311-1324.

Gamboa, D. and Alves, T.M., 2015. Three-dimensional fault meshes and multi-layer shear in mass-transport blocks: Implications for fluid flow on continental margins. Tectonophysics, 647–648(0): 21-32.

Gee, M.J.R., Gawthorpe, R.L. and Friedmann, S.J., 2006. Triggering and Evolution of a Giant Submarine Landslide, Offshore Angola, Revealed by 3D Seismic Stratigraphy and Geomorphology. Journal of Sedimentary Research, 76(1): 9-19.

Giles, K.A. and Lawton, T.F., 2002. Halokinetic sequence stratigraphy adjacent to the El Papalote diapir, northeastern Mexico. AAPG bulletin, 86(5): 823-840.

Giles, K.A. and Rowan, M.G., 2012. Concepts in halokinetic-sequence deformation and stratigraphy. In: G.I. Alsop, S.G. Archer, A.J. Hartley, N.T. Grant and R. Hodgkinson (Eds.), Salt Tectonics, Sediments and Prospectivity, Geological Society, London, Special Publications 363, London, pp. 7-31.

Hampton, M.A., Lee, H.J. and Locat, J., 1996. Submarine Landslides. Review of Geophysics, 34(1): 33-59.

Jackson, C.A.-L., 2012. The initiation of submarine slope failure and the emplacement of mass transport complexes in salt-related minibasins: A three-dimensional seismic-reflection case study from the Santos Basin, offshore Brazil. Geological Society of America Bulletin, 124(5-6): 746-761.

Jackson, M.P.A., Vendeville, B. and Schultz-Ela, D.D., 1994. Structural Dynamics of Salt Systems. Annual Review Of Earth And Planetary Sciences, 22: 93-117.

Klar, A., Aharonov, E., Kalderon Asael, B. and Katz, O., 2011. Analytical and observational relations between landslide volume and surface area. Journal of Geophysical Research: Earth Surface, 116(F2).

Kvalstad, T.J. et al., 2005. The Storegga slide: evaluation of triggering sources and slide mechanics. Marine and Petroleum Geology, 22(1–2): 245-256.

Lee, H.J., 2009. Timing of occurrence of large submarine landslides on the Atlantic Ocean margin. Marine Geology, 264(1-2): 53-64.

Love, F. et al., 2005. Northern Espírito Santo basin canyon models ancient sand transport. Offshore, March 2005: 74-78.

Madof, A.S., Christie-Blick, N. and Anders, M.H., 2009. Stratigraphic controls on a salt-withdrawal intraslope minibasin, north-central Green Canyon, Gulf of Mexico: Implications for misinterpreting sea level change. AAPG bulletin, 93(4): 535-561.

Maia, A., Cartwright, J., Andersen, E. and Gamboa, D., 2015. Fluid flow within MTDs: Evidences of fluid storage and leakage from 3D seismic data, offshore West Africa, 7th International Symposium of Submarine Mass Movements and Their Consequences, Wellington, NZ.

Masson, D.G., Harbitz, C.B., Wynn, R.B., Pedersen, G. and Løvholt, F., 2006. Submarine landslides: Processes, triggers and hazard prediction. Philosophical Transactions: Mathematical, Physical and Engineering Sciences (Series A), 364(1845): 2009-2039.

Micallef, A., Berndt, C., Masson, D.G. and Stow, D.A., 2008. Scale invariant characteristics of the Storegga Slide and implications for large-scale submarine mass movements. Marine Geology, 247(1): 46-60.

Moernaut, J. and De Batist, M., 2011. Frontal emplacement and mobility of sublacustrine landslides: Results from morphometric and seismostratigraphic analysis. Marine Geology, 285(1–4): 29-45.

Mohriak, W.U., 1995. Salt tectonics structural styles: contrasts and similarities between the South Atlantic and the Gulf of Mexico. In: C.J. Travis et al. (Eds.), Salt, Sediment and Hydrocarbons, Gulf Coast Section of the Society of Economic Paleontologists and Mineralogists (GCSSEPM Foundation), 16th Annual Research Conference, Houston, Texas, pp. 177-191.

Mohriak, W.U., 2003. Bacias sedimentares da margem continental Brasileira. In: L.A. Bizzi, C. Schobbenhaus, R.M. Vidotti and J.H. Goncalves (Eds.), Geologia, Tectonica e Recursos Minerais do Brasil. CPRM, Brasilia, pp. 87-165.

Moreira, J.L.P. and Carminatti, M., 2004. Sistemas deposicionais de talude e de bacia no Eoceno da Bacia de Santos. Boletim de Geociências da Petrobras, 12(1): 73-87.

Moscardelli, L. and Wood, L., 2008. New classification system for mass transport complexes in offshore Trinidad. Basin Research, 20(1): 73-98.

Moscardelli, L. and Wood, L., 2015. Morphometry of mass-transport deposits as a predictive tool. Geological Society of America Bulletin: B31221. 1.

Nemec, W., 1991. Aspects of sediment movement on steep delta slopes. In: A. Colella and D.B. Prior (Eds.), Coarse-Grained Deltas: International Association of Sedimentologists Special Publication 10, pp. 29–73.

O'Leary, D., 1991. Structure and morphology of submarine slab slides: clues to origin and behavior. Marine Georesources & Geotechnology, 10(1-2): 53-69.

Ogata, K., Mountjoy, J.J., Pini, G.A., Festa, A. and Tinterri, R., 2014. Shear zone liquefaction in mass transport deposit emplacement: A multi-scale integration of seismic reflection and outcrop data. Marine Geology, 356(0): 50-64.

Olafiranye, K., Jackson, C.A.-L. and Hodgson, D.M., 2013. The role of tectonics and mass-transport complex emplacement on upper slope stratigraphic evolution: A 3D seismic case study from offshore Angola. Marine and Petroleum Geology, 44: 196-216.

Omosanya, K.d.O. and Alves, T.M., 2013a. Ramps and flats of mass-transport deposits (MTDs) as markers of seafloor strain on the flanks of rising diapirs (Espírito Santo Basin, SE Brazil). Marine Geology, 340(0): 82-97.

Omosanya, K.O. and Alves, T.M., 2013b. A 3-dimensional seismic method to assess the provenance of Mass-Transport Deposits (MTDs) on salt-rich continental slopes (Espírito Santo Basin, SE Brazil). Marine and Petroleum Geology, 44: 223-239.

Posamentier, H. and Martinsen, O.J., 2011. The character and genesis of submarine mass-transport deposits: insights from outcrop and 3D seismic data. In: C. Shipp, P. Weimer and H. Posamentier (Eds.), Mass-transport deposits in deepwater settings. SEPM Special Publication 96, pp. 7-38.

Sultan, N. et al., 2004. Triggering mechanisms of slope instability processes and sediment failures on continental margins: a geotechnical approach. Marine Geology, 213(1-4): 291-321.

Tripsanas, E.K., Bryant, W.R. and Phaneuf, B.A., 2004. Slope-instability processes caused by salt movements in a complex deep-water environment, Bryant Canyon area, northwest Gulf of Mexico. AAPG bulletin, 88(6): 801-823.

Tripsanas, E.K., Piper, D.J.W., Jenner, K.A. and Bryant, W.R., 2008. Submarine mass-transport facies: new perspectives on flow processes from cores on the eastern North American margin. Sedimentology, 55(1): 97-136.

Varnes, D.J., 1978. Slope movement types and processes. Transportation Research Board Special Report(176).

Figures

Figure 1. a) Location of the Espírito Santo Basin on the SE Brazilian margin. **b)** Seafloor map of the salt-withdrawal minibasin here studied. Numerous MTDs occur on the seafloor, adjacent to N-S oriented salt ridges R1 and R2. Small axial slope failures and extensional cracks are also present towards the north. **c)** Stratigraphic chart of the Espírito Santo Basin showing the main depositional environments and tectonic phases (modified from França et al., 2007). The red box highlights the time intervals considered for this study.

Figure 2. Diagram showing the main stratigraphic mega-sequences in the Espírito Santo Basin and the styles of halokinetic structures across the slope. The study area is located on the distal basin domains where compressive salt structures predominate. Modified after Fiduk et al. (2004) and Gamboa et al. (2010).

Figure 3. a and **b**) Uninterpreted and interpreted seismic sections along and across the minibasin. The buried MTDs here analysed occur in the interval delimited by horizons H1 and H4. Extensional faults tend to prevail in the northern areas of the minibasin, greatly decreasing their frequency southwards. **c)** 3D fence diagrams showing the lateral continuity of the interpreted horizons in the whole minibasin, within and outside the MTDs.

Figure 4. a) Thickness map of interval H1-H4. The main thickness heterogeneities observed are due to the presence of the MTDs. **b**) Variance slice 16 ms above horizon H1, the basal surface of buried MTDs. The MTDs are evidenced by marked variance heterogeneities within delimited areas. **c**) Variance slice 16 ms below horizon H1 showing the distribution of faults in the minibasin.

Figure 5. a, **b** and **c**) Seismic profiles intersecting MTD A, which is delimited and underlain by numerous faults. **d**) 3D surface of horizon H3, the top of MTD A. Numerous ridges and faults are observed, with relevance for mid-MTD secondary compressional and extensional domains.

Figure 6. a) Morphologic profiles of H1 and H3. **b**) Thickness map of MTD A. Strata thickening is associated with the compressional domains. **c**) Variance slice showing the internal heterogeneity of MTD A, evidencing numerous arcuate faults and ridges. **d**) RMS amplitude map of MTD A. Lower amplitudes predominating on the thinned extensional domains and on the western part of the MTD toe.

Figure 7. a) Seismic profile along MTD B, adjacent to salt ridge R2. Thrust structures and associated compressional ridges are frequent at the front of the deposit, confined by a frontal ramp. Seismic reflections are well-preserved in the compressional domain when compared to the disrupted upslope areas. **b**) 3D surface of the top of MTD B. **c**) thickness map of MTD B. Localised thickening upslope occurs within the erosive slot. **d**) variance slice within MTD B. No sharp headwall scarp is observed for this deposit. **e**) RMS amplitude map, showing amplitude heterogeneities that reflect the deformation ridges of MTD B.

Figure 8. Seismic sections along and across MTD C. **a)** section sub-parallel to the MTD long axis crossing the low deformation slabs. **b)** section showing upslope strata buttressing against an MTD slab, and compressional pop-up blocks at the toe domain. The large slabs show negligent internal deformation **c)** depiction of numerous extensional faults on the upslope domain, possibly resultant from retrogressive failures, followed by a slab and compressional structures downslope. **d)** evidence of well-developed compressive ridges at mid-MTD positions. **e)** section showing the headwall controlled by ridge R1, and indicators of possible thrusts within the moving slabs.

Figure 9. a) 3D surface of the top of MTD C. **b**) Profile of the base and top horizons of MTD C. The rugosity of the top surface is related to its internal deformation, with smooth profiles on top of slabs and marked irregularities on the evacuation and toe domains. **c)** Thickness map of MTD C. **d**) Variance slice within MTD C. The slabs show uniform patterns, identical to the unremobilised strata outside the MTD. Compressional ridges are well evidenced not only at the toe, but also at mid-MTD locations. **e**) RMS amplitude map of MTD C, showing predominantly low amplitudes at the headwall domain.

Figure 10. a) 3D gradient surface of MTD SF1, showing elongated slabs followed downslope by compressive ridges. The headwall scarp is clearly observed, with adjacent rotational blocks. **b**) 3D gradient surface of MTDs SF2 and SF3. **c**) Seismic section across MTD SF1, showing preserved reflections in the slab and imbricated thrusts at the toe. **d**) Thickness map of SF1. **e)** seismic section along SF2. The bulk of the MTD shows internal thrusting delimited by a frontal ramp, followed downslope by a thin emergent lobe. **f**) Thickness map of SF2, showing the thickening at the compressional domain and the markedly thinner frontal love. **g** and **h**) Seismic section and thickness map of SF3, which shows a character is similar to SF2.

Figure 11. a) 3D gradient surface of MTD SF4. A complex headwall delimits SF4 upslope, evidencing two main scarp depths (2045 m and 2100 m) on the flank of ridge R2. **b**) Seismic section across SF4. Distal deformation of the seismic reflections within the MTD is very limited, being only inferred from subtle thickness changes and reflection irregularities.

Figure 12. Plots of the relationships between MTD morphological parameters. **a**) ratios between the long and short axes of MTDs. **b**) measured values for the long and short MTD axes. **c**) Relationship between the MTD volume and area. **d**) Volumes and area of slabs in MTD C, showing a very close relationship between both parameters. **e**) Comparison between the size of the slabs in the detached MTDs and blocks in attached MTDs in the Espírito Santo Basin. **f** and **g)** plots representing the relationship between the headwall length versus the area and the volume of the studied MTDs. **h**) MTD scarp length-distance to toe ratio.

Figure 13. a) Schematic diagram of the internal features interpreted in Type 1 MTDs. Internal deformation is predominantly medium to high. **b**) Schematic diagram of the deformation of Type 2 MTDs, with emphasis for the low deformation slabs. HL: Headwall Length, DtT: Distance-to-toe.

Figure 14. Interpreted timing of basin deformation episodes indicated by MTDs. **a**) MTDs detaching along horizon H1. 1-Deposition of H1 to H3, no significant instability; 2-Localised subsidence and fault movement. Triggering of MTD A, deforming the paleo-seafloor (H3). 3- Deposition of H4. 4- Instability along salt ridges towards the south and triggering of MTDs B and C. **b**) Modern seafloor MTDs. 1- Instability along R2 and initial deposits of SF4; 2- Local instability leading to various slope failures on both flanks of R1; 3-Smaller slope failures along R2, and minor subsidence on the northern axial areas.

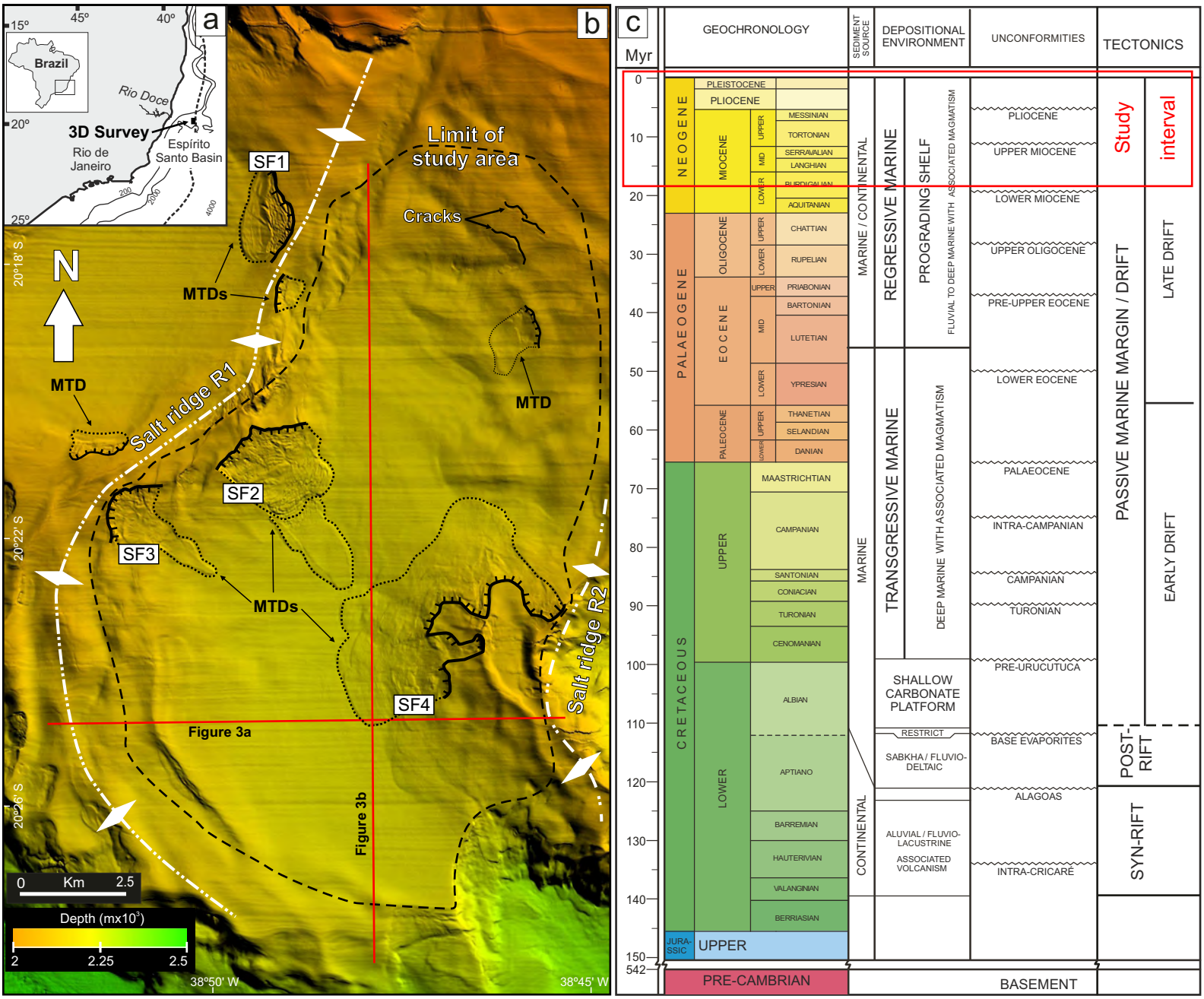
a
15°
45°
40°
Brazil
Rio Doce
20°
3D Survey
Rio de Janeiro
Espírito Santo Basin
200
2000
4000
25°
b
Limit of study area
Cracks
SF1
MTDs
N
MTD
Salt ridge R1
MTD
SF2
SF3
MTDs
Salt ridge R2
SF4
Figure 3a
Figure 3b
20°18' S
20°22' S
20°26' S
0 Km 2.5
Depth (mx10³)
2
2.25
2.5
38°50' W
38°45' W
c
Myr
GEOCHRONOLOGY
SEDIMENT SOURCE
DEPOSITIONAL ENVIRONMENT
UNCONFORMITIES
TECTONICS
0
10
20
30
40
50
60
70
80
90
100
110
120
130
140
150
542
NEOGENE
PLEISTOCENE
PLIOCENE
MIOCENE
UPPER
MID
LOWER
MESSINIAN
TORTONIAN
SERRAVALIAN
LANGHIAN
BURDIGALIAN
AQUITANIAN
PALAEOGENE
OLIGOCENE
CHATTIAN
RUPELIAN
EOCENE
PRIABONIAN
BARTONIAN
LUTETIAN
YPRESIAN
PALEOCENE
THANETIAN
SELANDIAN
DANIAN
CRETACEOUS
MAASTRICHTIAN
CAMPANIAN
SANTONIAN
CONIACIAN
TURONIAN
CENOMANIAN
ALBIAN
APTIANO
BARREMIAN
HAUTERIVIAN
VALANGINIAN
BERRIASIAN
JURASSIC
PRE-CAMBRIAN
MARINE / CONTINENTAL
MARINE
CONTINENTAL
REGRESSIVE MARINE
PROGRADING SHELF
FLUVIAL TO DEEP MARINE WITH ASSOCIATED MAGMATISM
TRANSGRESSIVE MARINE
DEEP MARINE WITH ASSOCIATED MAGMATISM
SHALLOW CARBONATE PLATFORM
RESTRICT
SABKHA / FLUVIO-DELTAIC
ALUVIAL / FLUVIO-LACUSTRINE
ASSOCIATED VOLCANISM
PLIOCENE
UPPER MIOCENE
LOWER MIOCENE
UPPER OLIGOCENE
PRE-UPPER EOCENE
LOWER EOCENE
PALAEOCENE
INTRA-CAMPANIAN
CAMPANIAN
TURONIAN
PRE-URUCUTUCA
BASE EVAPORITES
ALAGOAS
INTRA-CRICARÉ
BASEMENT
Study interval
PASSIVE MARINE MARGIN / DRIFT
LATE DRIFT
EARLY DRIFT
POST-RIFT
SYN-RIFT

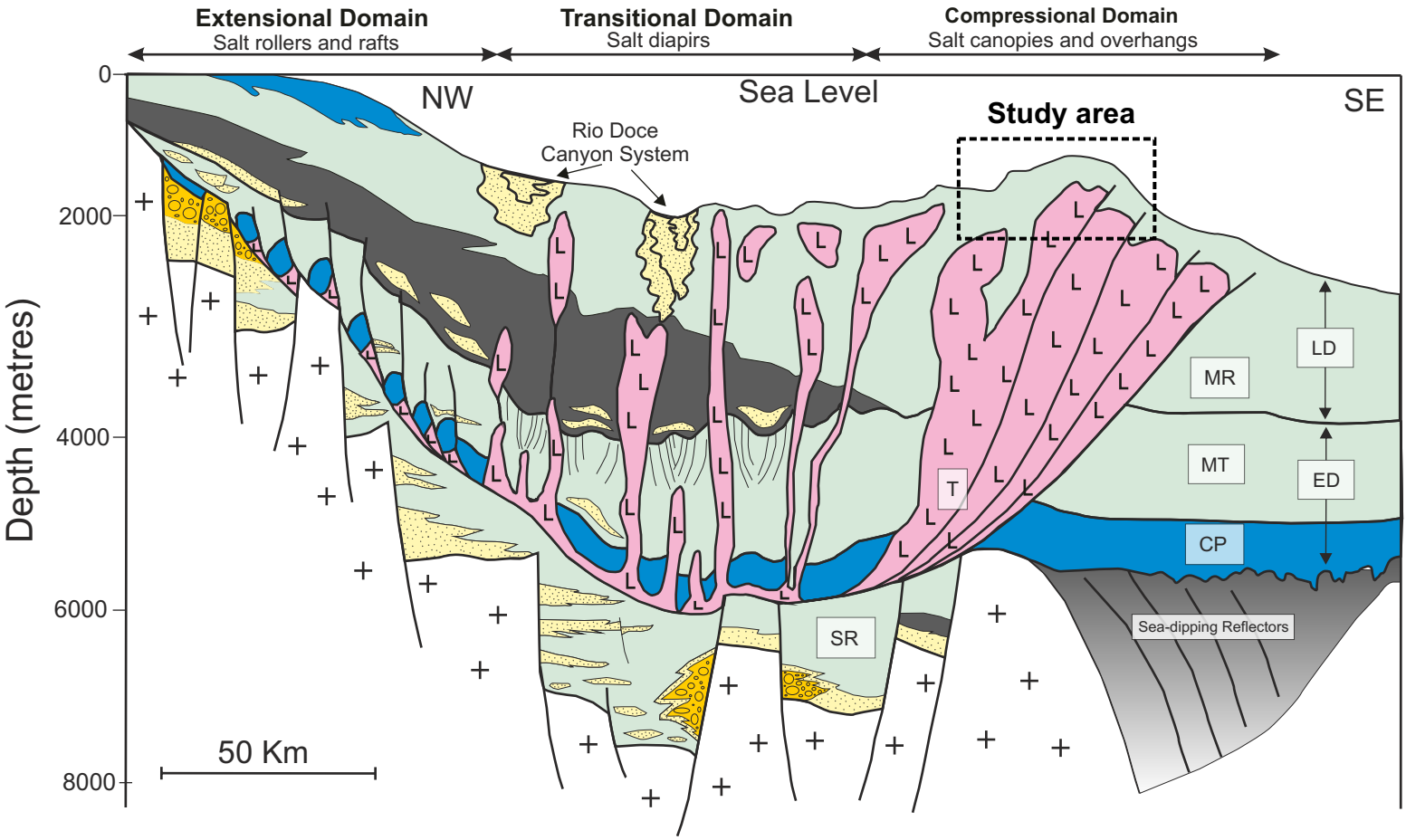

Lithology

- Carbonate
- Conglomerate
- Sandstone
- Basement
- Shale/marl
- Evaporites
- MTD/Volcaniclastic

Sequence Key

SR	-Syn-Rift		
T	-Transitional		
ED	-Early Drift	CP	-Carbonate Platform
		MT	-Marine Transgressive
LD	-Late Drift	MR	-Marine Regressive

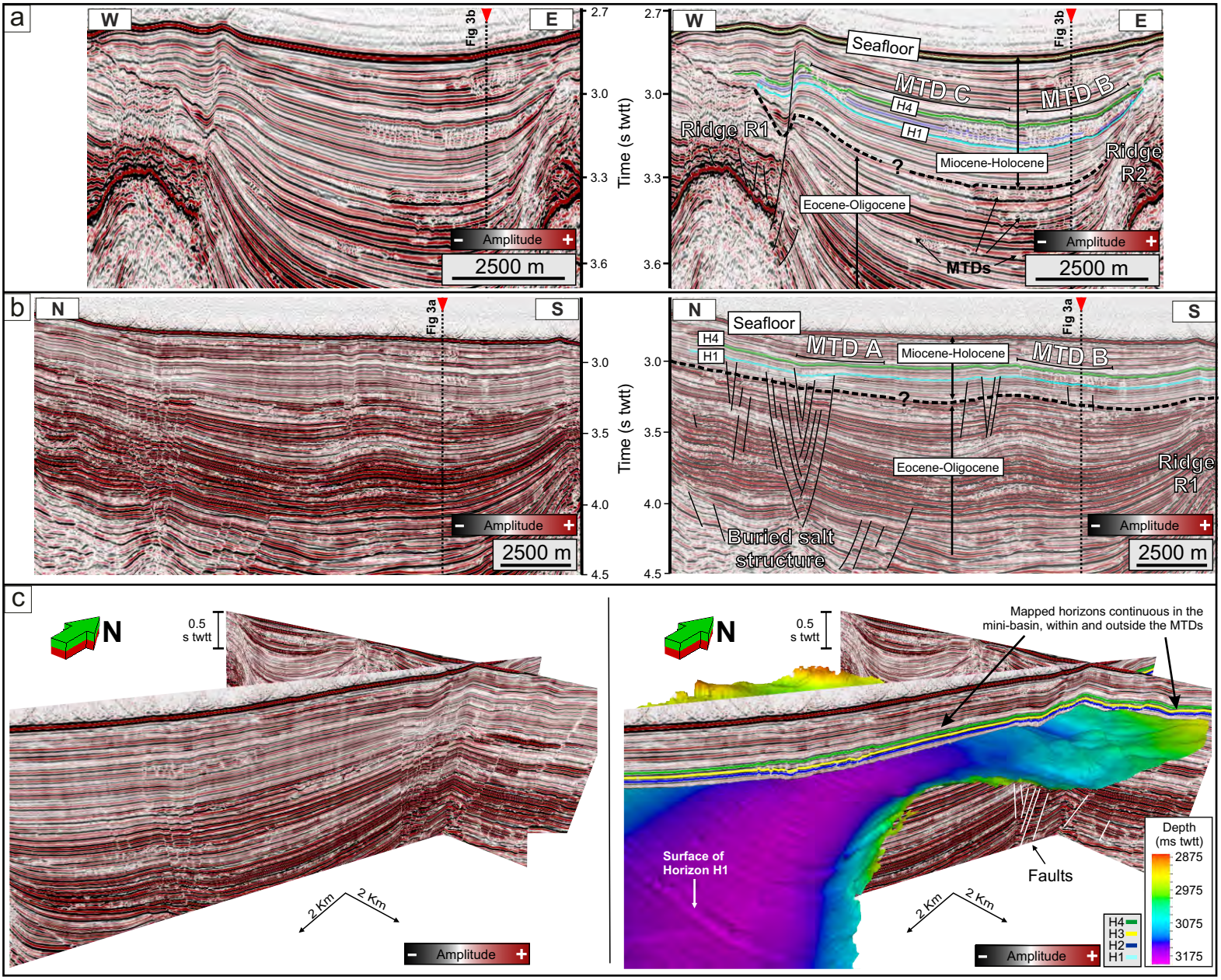
a
W
E
Fig 3b
Amplitude
2500 m
Time (s twtt)
2.7
3.0
3.3
3.6
Seafloor
MTD C
MTD B
H4
H1
Ridge R1
Ridge R2
Miocene-Holocene
Eocene-Oligocene
MTDs
b
N
S
Fig 3a
MTD A
Buried salt structure
c
0.5 s twtt
2 Km
Surface of Horizon H1
Mapped horizons continuous in the mini-basin, within and outside the MTDs
Faults
Depth (ms twtt)
2875
2975
3075
3175
H4
H3
H2
H1

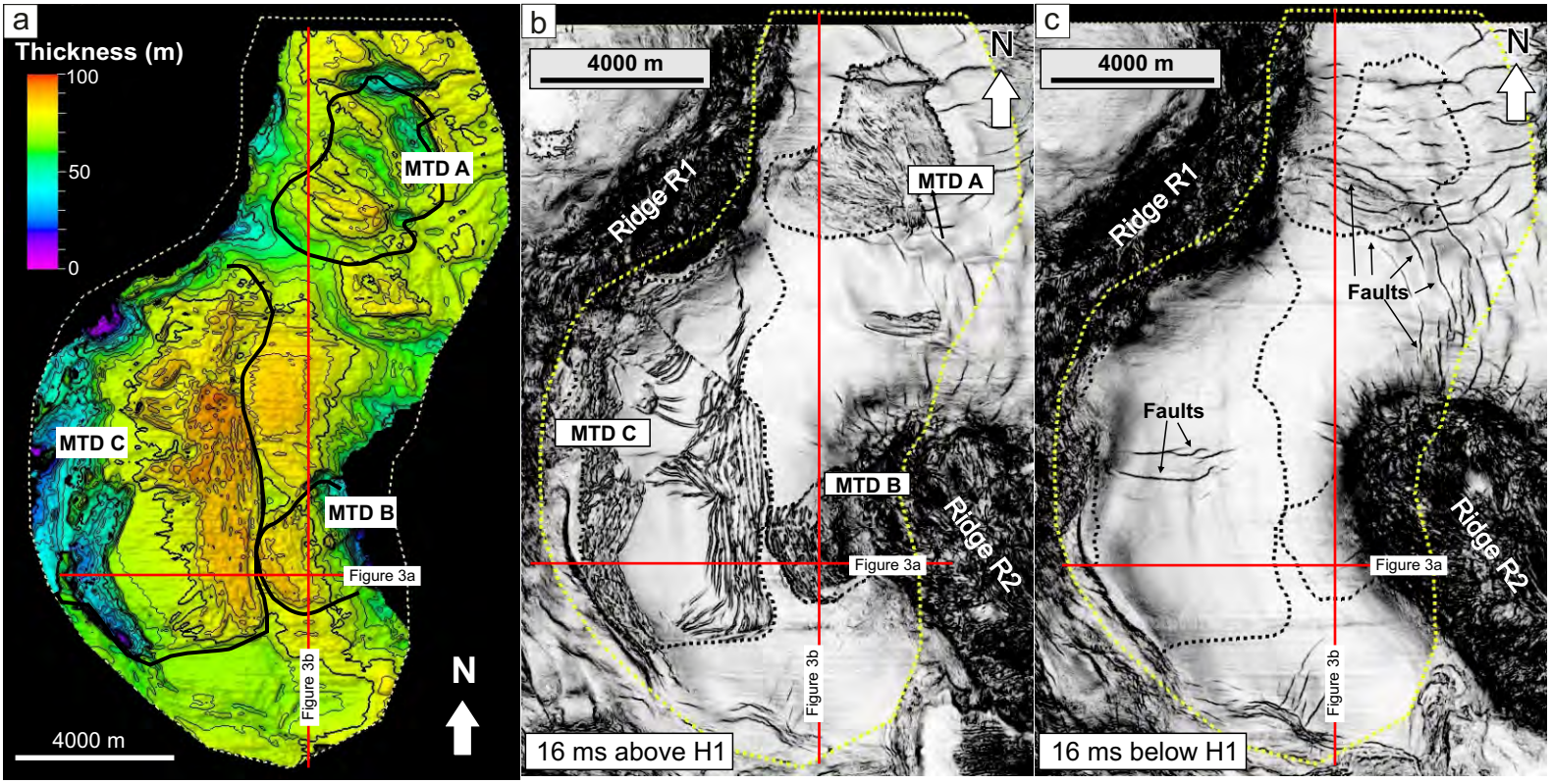
a
Thickness (m)
100
50
0
MTD A
MTD C
MTD B
Figure 3a
Figure 3b
N
4000 m
b
4000 m
N
Ridge R1
MTD A
MTD C
MTD B
Ridge R2
Figure 3a
Figure 3b
16 ms above H1
c
4000 m
N
Ridge R1
Faults
Faults
Ridge R2
Figure 3a
Figure 3b
16 ms below H1

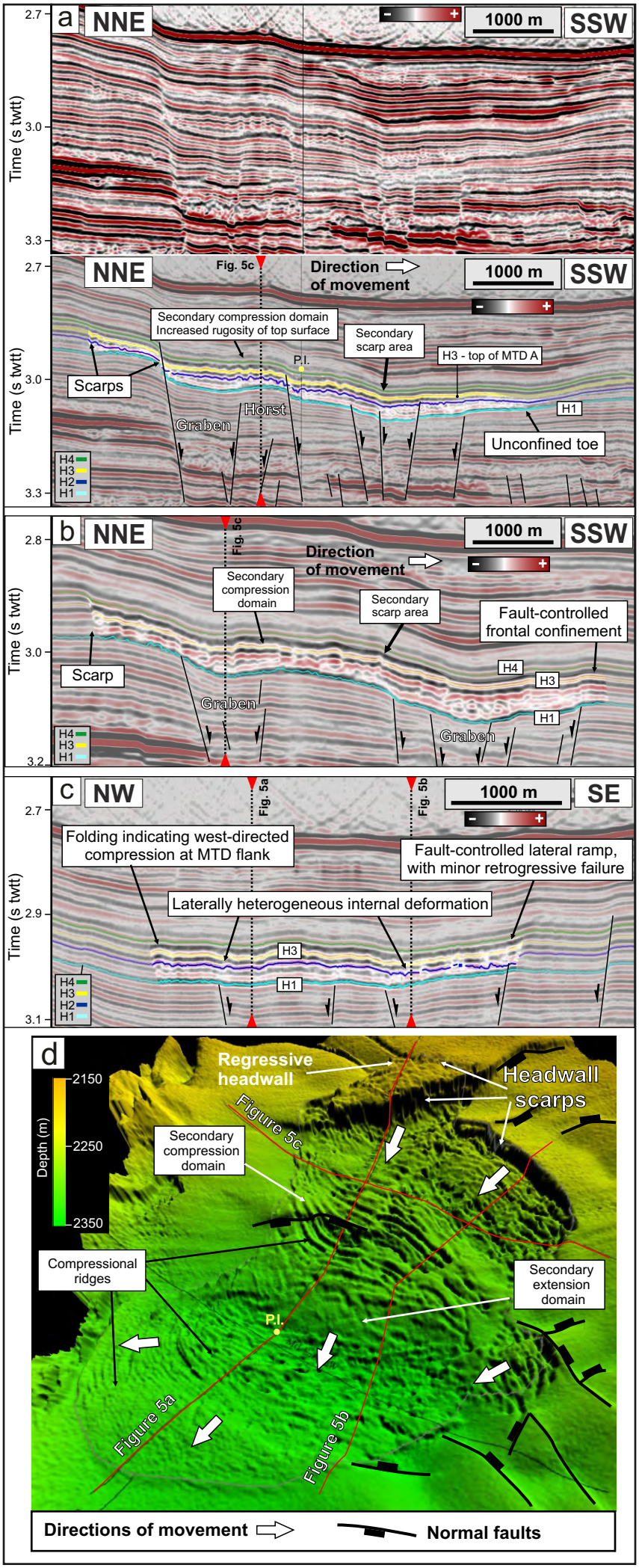
a
NNE
SSW
1000 m
Time (s twtt)
2.7
3.0
3.3
NNE
Fig. 5c
Direction of movement
SSW
1000 m
Secondary compression domain
Increased rugosity of top surface
Secondary scarp area
H3 - top of MTD A
Scarps
P.I.
Horst
Graben
H1
Unconfined toe
H4
H3
H2
H1
b
NNE
Fig. 5c
1000 m
SSW
Direction of movement
Secondary compression domain
Secondary scarp area
Fault-controlled frontal confinement
Scarp
H4
H3
Graben
H1
Graben
2.8
3.0
3.2
c
NW
Fig. 5a
Fig. 5b
1000 m
SE
Folding indicating west-directed compression at MTD flank
Fault-controlled lateral ramp, with minor retrogressive failure
Laterally heterogeneous internal deformation
H3
H1
2.7
2.9
3.1
d
Depth (m)
2150
2250
2350
Regressive headwall
Headwall scarps
Figure 5c
Secondary compression domain
Compressional ridges
Secondary extension domain
P.I.
Figure 5a
Figure 5b
Directions of movement
Normal faults

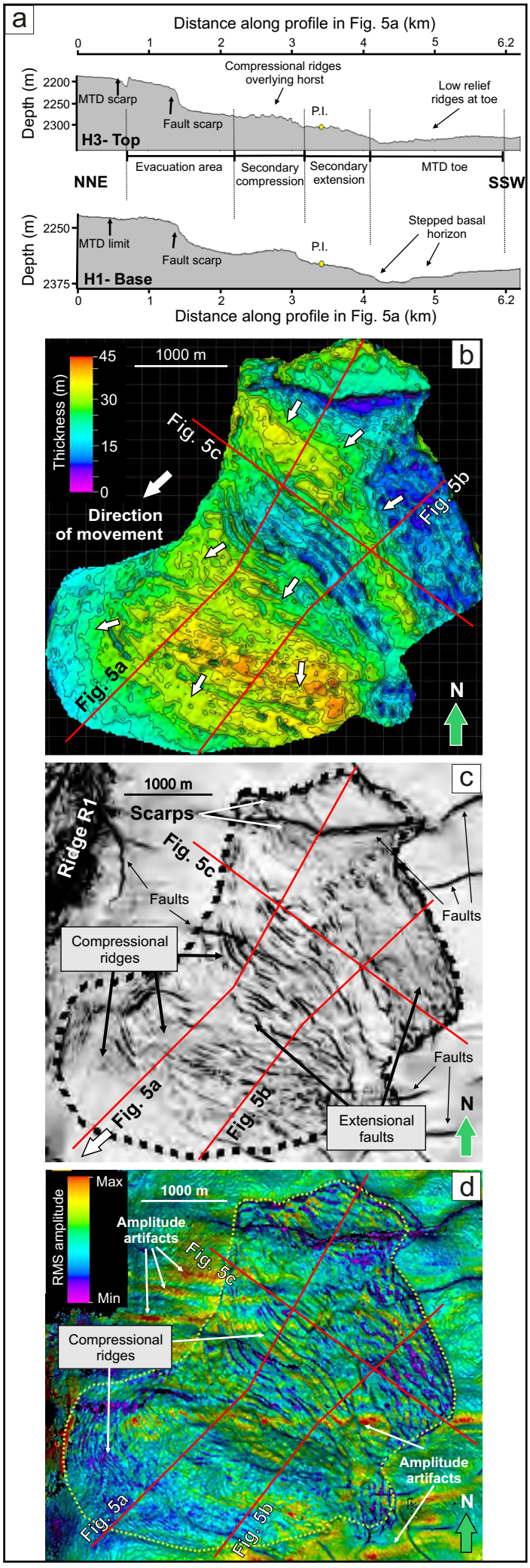
a
Distance along profile in Fig. 5a (km)
0
1
2
3
4
5
6.2
Depth (m)
2200
2250
2300
MTD scarp
Fault scarp
Compressional ridges overlying horst
P.I.
Low relief ridges at toe
H3- Top
Evacuation area
Secondary compression
Secondary extension
MTD toe
NNE
SSW
2250
2375
MTD limit
Fault scarp
P.I.
Stepped basal horizon
H1- Base
Distance along profile in Fig. 5a (km)
b
Thickness (m)
45
30
15
0
1000 m
Fig. 5c
Fig. 5b
Direction of movement
Fig. 5a
N
c
1000 m
Ridge R1
Scarps
Fig. 5c
Faults
Faults
Compressional ridges
Faults
Fig. 5a
Fig. 5b
Extensional faults
N
d
RMS amplitude
Max
Min
1000 m
Amplitude artifacts
Fig. 5c
Compressional ridges
Amplitude artifacts
Fig. 5a
Fig. 5b
N

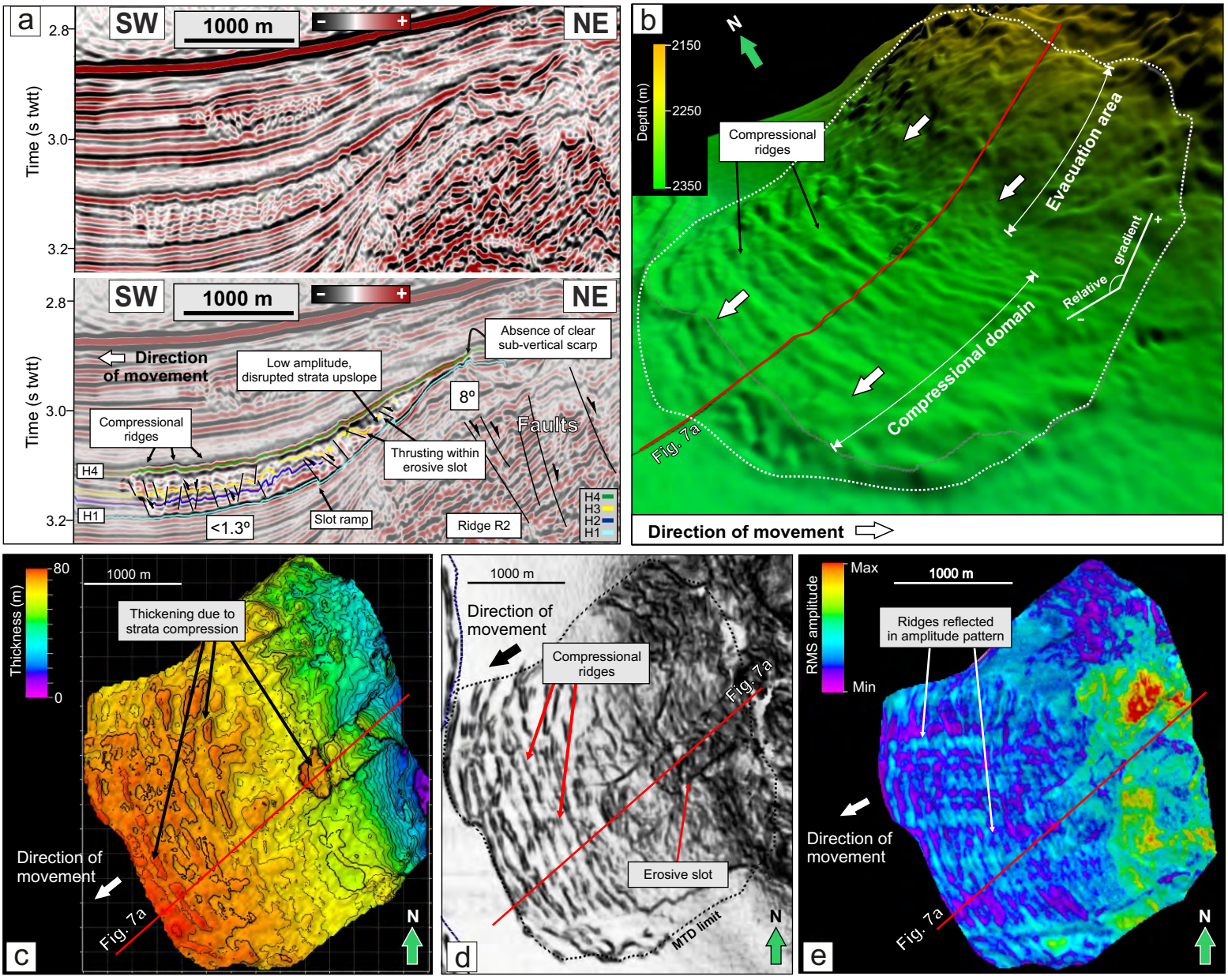
a
SW
1000 m
NE
Time (s twt)
2.8
3.0
3.2
Direction of movement
Low amplitude, disrupted strata upslope
Absence of clear sub-vertical scarp
8°
Compressional ridges
Faults
Thrusting within erosive slot
H4
H1
<1.3°
Slot ramp
Ridge R2
H4
H3
H2
H1
b
N
Depth (m)
2150
2250
2350
Compressional ridges
Evacuation area
Relative gradient
Compressional domain
Fig. 7a
Direction of movement
c
Thickness (m)
80
0
1000 m
Thickening due to strata compression
Direction of movement
Fig. 7a
N
d
1000 m
Direction of movement
Compressional ridges
Fig. 7a
Erosive slot
MTD limit
N
e
RMS amplitude
Max
Min
1000 m
Ridges reflected in amplitude pattern
Direction of movement
Fig. 7a
N

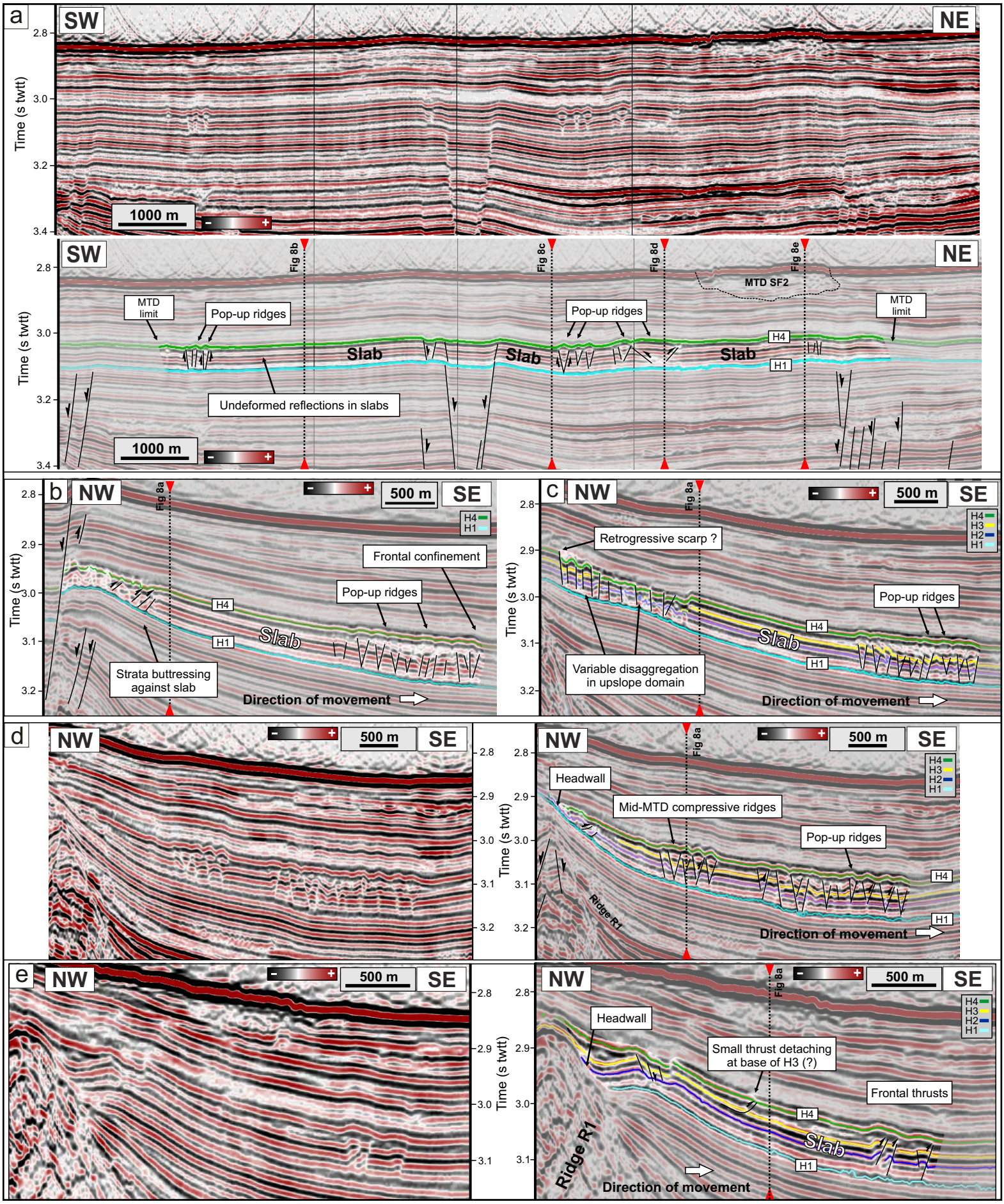
a
SW
NE
Time (s twtt)
2.8
3.0
3.2
3.4
1000 m
Fig 8b
Fig 8c
Fig 8d
Fig 8e
MTD SF2
MTD limit
Pop-up ridges
Slab
H4
H1
Undeformed reflections in slabs
b
NW
SE
500 m
Fig 8a
Frontal confinement
Strata buttressing against slab
Direction of movement
c
Retrogressive scarp ?
Variable disaggregation in upslope domain
H3
H2
d
Headwall
Mid-MTD compressive ridges
Ridge R1
e
Small thrust detaching at base of H3 (?)
Frontal thrusts

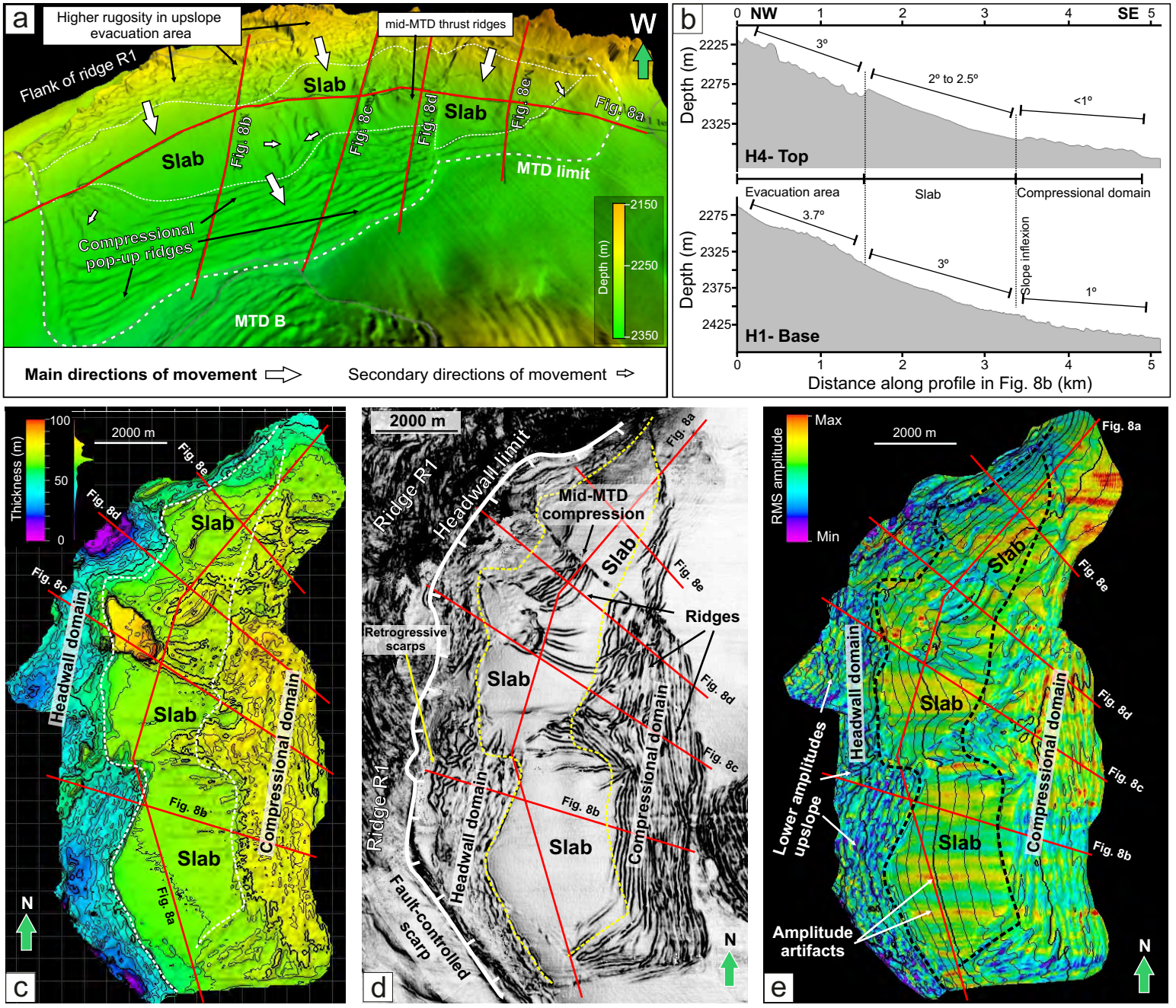
a
Higher rugosity in upslope evacuation area
mid-MTD thrust ridges
W
Flank of ridge R1
Slab
Slab
Slab
Fig. 8b
Fig. 8c
Fig. 8d
Fig. 8e
Fig. 8a
MTD limit
Compressional pop-up ridges
MTD B
Depth (m)
2150
2250
2350
Main directions of movement
Secondary directions of movement
b
NW
SE
Depth (m)
3°
2° to 2.5°
<1°
H4- Top
Evacuation area
Slab
Compressional domain
3.7°
3°
1°
Slope inflexion
H1- Base
Distance along profile in Fig. 8b (km)
c
Thickness (m)
100
50
0
2000 m
Fig. 8e
Fig. 8d
Fig. 8c
Fig. 8b
Fig. 8a
Slab
Slab
Slab
Headwall domain
Compressional domain
N
d
2000 m
Ridge R1
Headwall limit
Mid-MTD compression
Fig. 8a
Fig. 8e
Fig. 8d
Fig. 8c
Fig. 8b
Slab
Slab
Slab
Ridges
Retrogressive scarps
Ridge R1
Headwall domain
Compressional domain
Fault-controlled scarp
N
e
RMS amplitude
Max
Min
2000 m
Fig. 8a
Fig. 8e
Fig. 8d
Fig. 8c
Fig. 8b
Slab
Slab
Slab
Headwall domain
Compressional domain
Lower amplitudes upslope
Amplitude artifacts
N

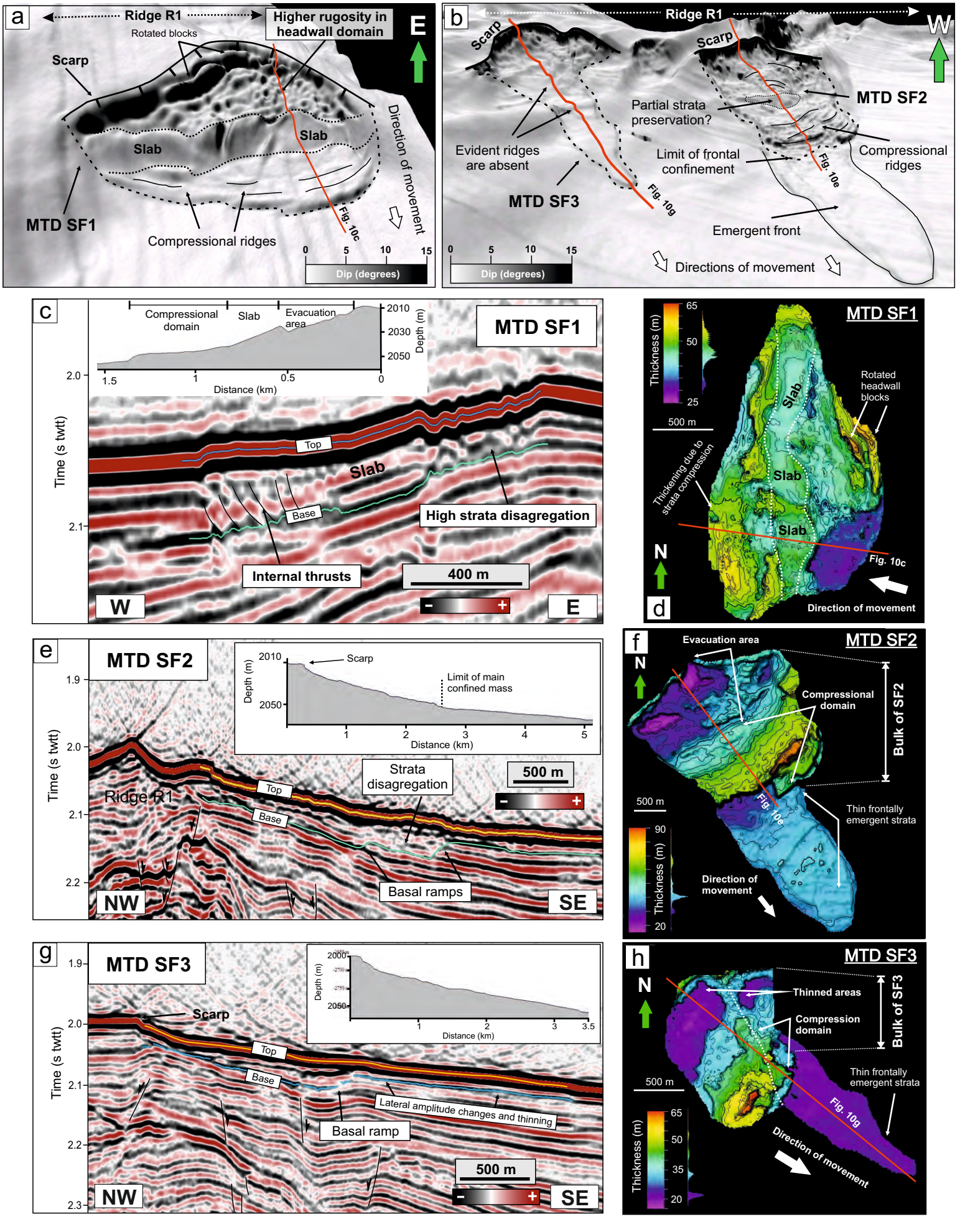
a
Ridge R1
Rotated blocks
Higher rugosity in headwall domain
E
Scarp
Slab
Slab
Direction of movement
MTD SF1
Compressional ridges
Fig. 10c
0 5 10 15
Dip (degrees)
b
Ridge R1
W
Scarp
Scarp
MTD SF2
Partial strata preservation?
Evident ridges are absent
Limit of frontal confinement
Compressional ridges
Fig. 10e
MTD SF3
Fig. 10g
Emergent front
0 5 10 15
Dip (degrees)
Directions of movement
c
Compressional domain
Slab
Evacuation area
2010
2030
2050
Depth (m)
1.5 1 0.5 0
Distance (km)
MTD SF1
2.0
Time (s twtt)
2.1
Top
Slab
Base
High strata disagregation
Internal thrusts
400 m
W
E
d
MTD SF1
65
50
25
Thickness (m)
500 m
Rotated headwall blocks
Slab
Thickening due to strata compression
Slab
Slab
N
Fig. 10c
Direction of movement
e
MTD SF2
2010
2050
Depth (m)
Scarp
Limit of main confined mass
1 2 3 4 5
Distance (km)
1.9
2.0
Time (s twtt)
2.1
2.2
Ridge R1
Top
Base
Strata disagregation
500 m
Basal ramps
NW
SE
f
Evacuation area
MTD SF2
N
Compressional domain
Bulk of SF2
500 m
Fig. 10e
Thin frontally emergent strata
90
Thickness (m)
20
Direction of movement
g
MTD SF3
1.9
2.0
Time (s twtt)
2.1
2.2
2.3
Scarp
2000
2050
Depth (m)
1 2 3 3.5
Distance (km)
Top
Base
Lateral amplitude changes and thinning
Basal ramp
500 m
NW
SE
h
MTD SF3
N
Thinned areas
Compression domain
Bulk of SF3
500 m
Thin frontally emergent strata
Fig. 10g
65
50
35
20
Thickness (m)
Direction of movement

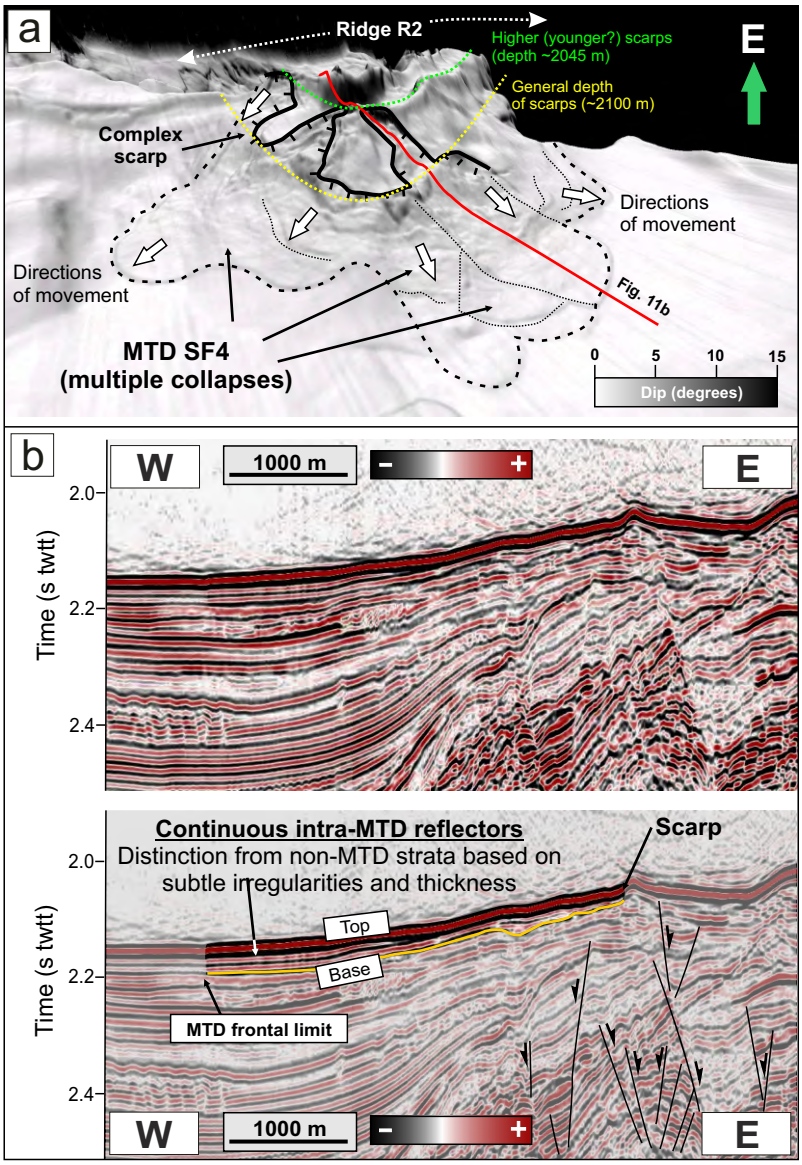
a
Ridge R2
Higher (younger?) scarps
(depth ~2045 m)
General depth
of scarps (~2100 m)
E
Complex
scarp
Directions
of movement
Directions
of movement
Fig. 11b
MTD SF4
(multiple collapses)
0
5
10
15
Dip (degrees)
b
W
1000 m
-
+
E
Time (s twtt)
2.0
2.2
2.4
Continuous intra-MTD reflectors
Distinction from non-MTD strata based on
subtle irregularities and thickness
Scarp
Top
Base
MTD frontal limit
W
1000 m
-
+
E

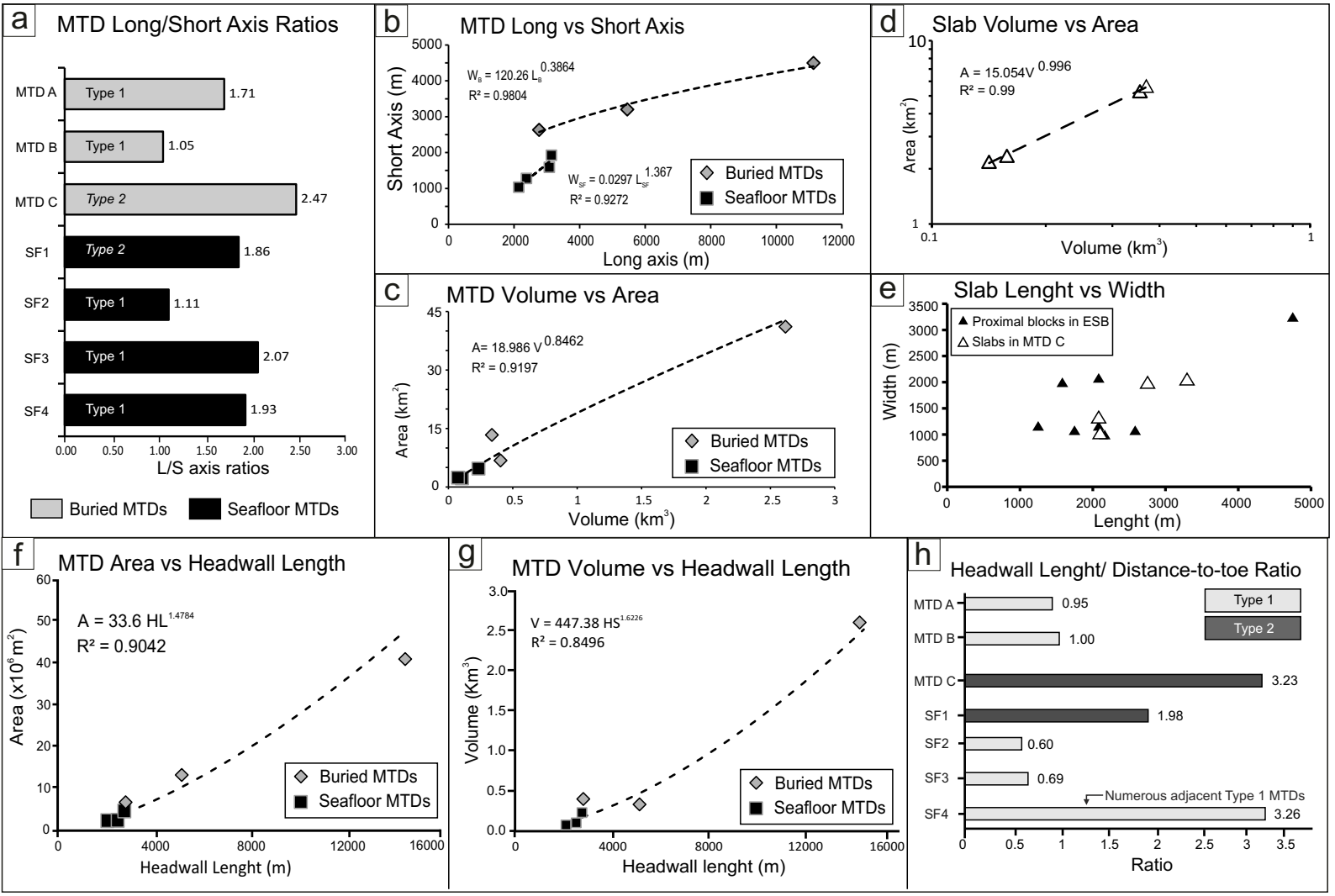
a
MTD Long/Short Axis Ratios
MTD A
Type 1
1.71
MTD B
Type 1
1.05
MTD C
Type 2
2.47
SF1
Type 2
1.86
SF2
Type 1
1.11
SF3
Type 1
2.07
SF4
Type 1
1.93
0.00 0.50 1.00 1.50 2.00 2.50 3.00
L/S axis ratios
Buried MTDs
Seafloor MTDs
b
MTD Long vs Short Axis
$W_B = 120.26\ L_B^{0.3864}$
$R^2 = 0.9804$
$W_{SF} = 0.0297\ L_{SF}^{1.367}$
$R^2 = 0.9272$
Short Axis (m)
Long axis (m)
Buried MTDs
Seafloor MTDs
c
MTD Volume vs Area
$A = 18.986\ V^{0.8462}$
$R^2 = 0.9197$
Area (km²)
Volume (km³)
Buried MTDs
Seafloor MTDs
d
Slab Volume vs Area
$A = 15.054V^{0.996}$
$R^2 = 0.99$
Area (km²)
Volume (km³)
e
Slab Lenght vs Width
Proximal blocks in ESB
Slabs in MTD C
Width (m)
Lenght (m)
f
MTD Area vs Headwall Length
$A = 33.6\ HL^{1.4784}$
$R^2 = 0.9042$
Area (x10⁶ m²)
Headwall Lenght (m)
Buried MTDs
Seafloor MTDs
g
MTD Volume vs Headwall Length
$V = 447.38\ HS^{1.6226}$
$R^2 = 0.8496$
Volume (Km³)
Headwall lenght (m)
Buried MTDs
Seafloor MTDs
h
Headwall Lenght/ Distance-to-toe Ratio
Type 1
Type 2
MTD A 0.95
MTD B 1.00
MTD C 3.23
SF1 1.98
SF2 0.60
SF3 0.69
SF4 3.26
Numerous adjacent Type 1 MTDs
Ratio

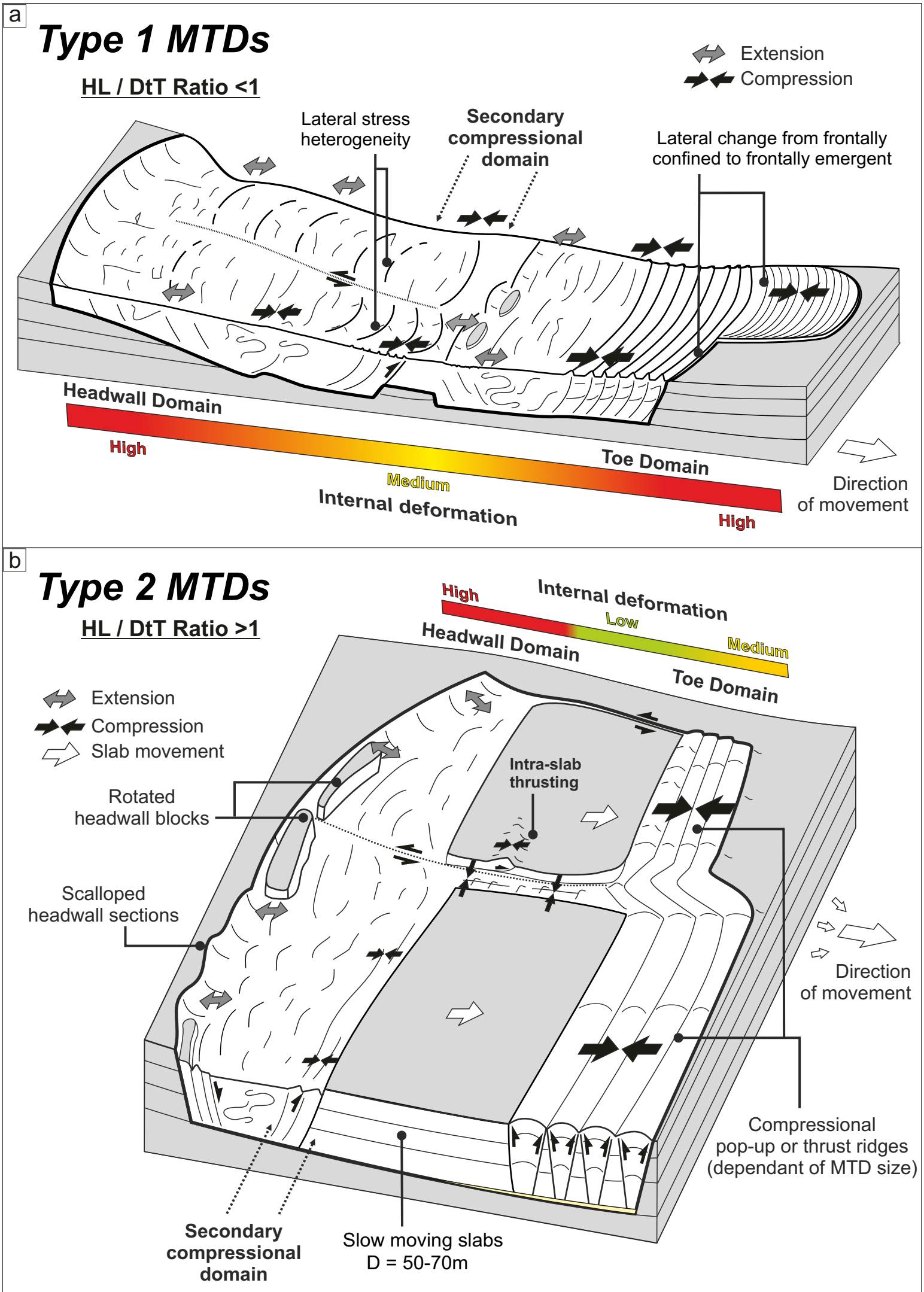
a
Type 1 MTDs
HL / DtT Ratio <1
Extension
Compression
Lateral stress heterogeneity
Secondary compressional domain
Lateral change from frontally confined to frontally emergent
Headwall Domain
High
Medium
Toe Domain
Internal deformation
High
Direction of movement
b
Type 2 MTDs
HL / DtT Ratio >1
High
Internal deformation
Low
Medium
Headwall Domain
Toe Domain
Extension
Compression
Slab movement
Intra-slab thrusting
Rotated headwall blocks
Scalloped headwall sections
Direction of movement
Compressional pop-up or thrust ridges (dependant of MTD size)
Secondary compressional domain
Slow moving slabs
D = 50-70m

a **Estimated timing of MTDs detaching along horizon H1**

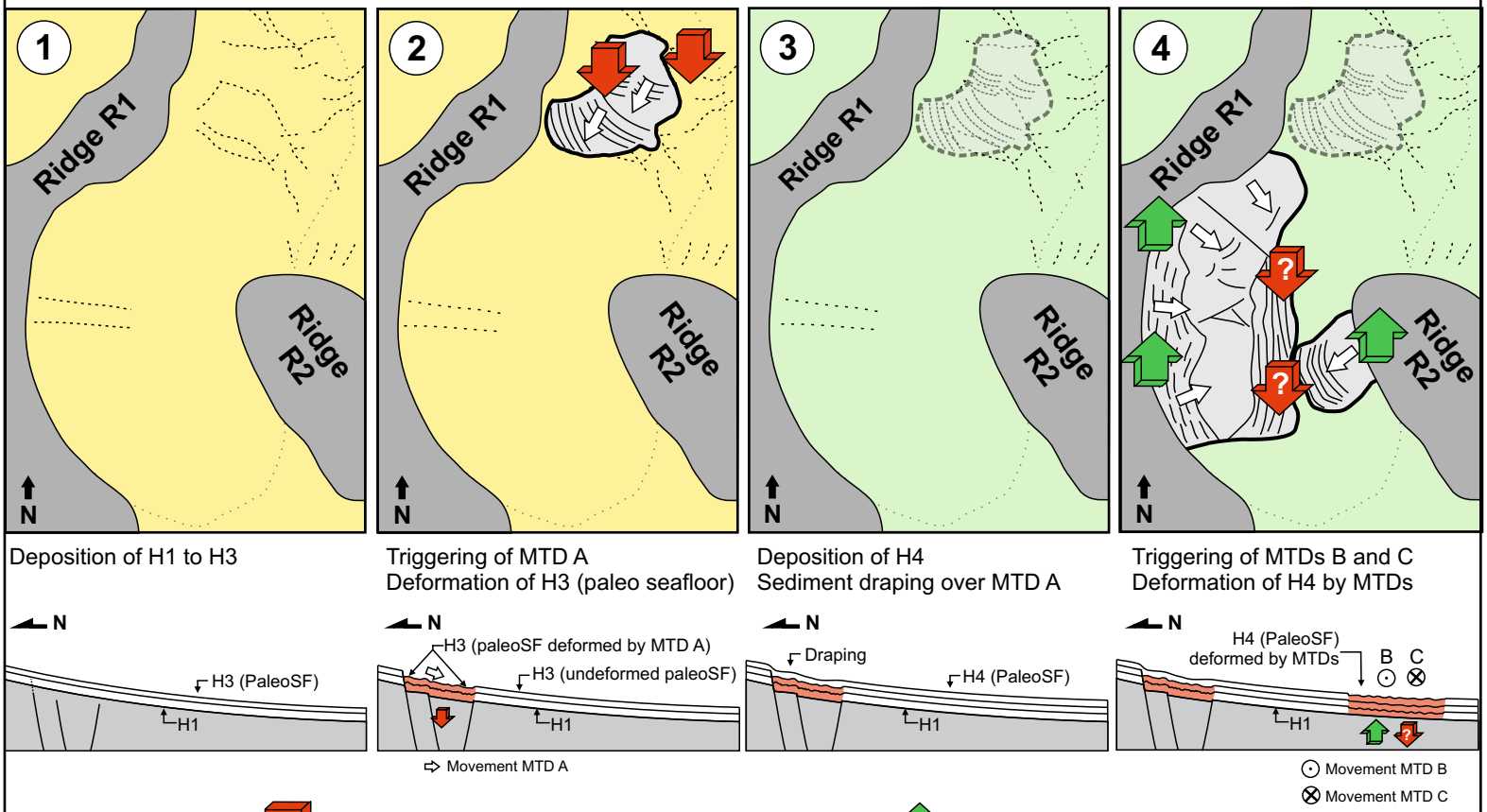

Deposition of H1 to H3

Triggering of MTD A
Deformation of H3 (paleo seafloor)

Deposition of H4
Sediment draping over MTD A

Triggering of MTDs B and C
Deformation of H4 by MTDs

Subsidence on basin axis

Uplift on salt ridges

b **Estimated timing of seafloor MTDs**

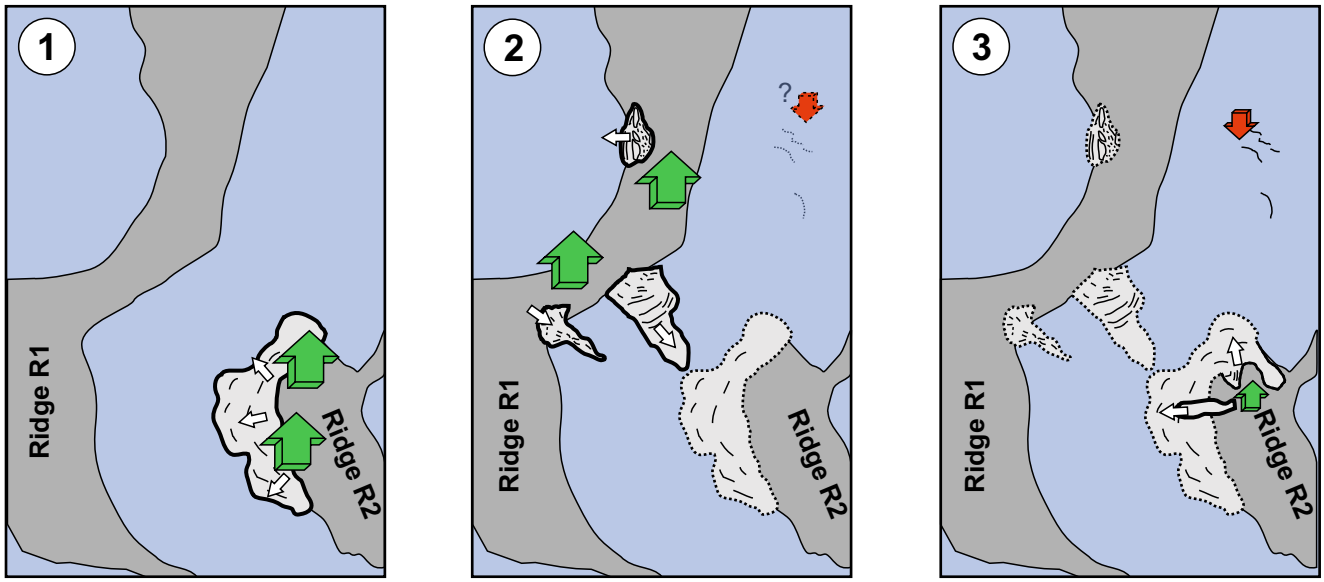

MTDs triggered along Ridge R2

MTDs triggered along Ridge R1

Smaller slope failures on ridge R2